Bromine-rich argyrodites compositions

Enhancing lithium-ion conductivity for improved solid-state battery performance

Shanbhag, Dhanush; Gautam, Ajay; Salager, Elodie; Albero-Blanquer, Laura; Marchini, Florencia; Chotard, Jean Noël; Fauth, François; Suard, Emmanuelle; Rabuel, François; More Authors

DOI
10.1016/j.jpowsour.2025.238175

Publication date
2025

Document Version
Final published version

Published in
Journal of Power Sources

Citation (APA)
Shanbhag, D., Gautam, A., Salager, E., Albero-Blanquer, L., Marchini, F., Chotard, J. N., Fauth, F., Suard, E., Rabuel, F., & More Authors (2025). Bromine-rich argyrodites compositions: Enhancing lithium-ion conductivity for improved solid-state battery performance. *Journal of Power Sources*, *657*, Article 238175. https://doi.org/10.1016/j.jpowsour.2025.238175

Journal of Power Sources 657 (2025) 238175

Contents lists available at ScienceDirect

Journal of Power Sources

journal homepage: www.elsevier.com/locate/jpowsour

Bromine-rich argyrodites compositions: Enhancing lithium-ion conductivity for improved solid-state battery performance

Dhanush Shanbhag [a,b,c], Ajay Gautam [d], Elodie Salager [b,e], Laura Albero-Blanquer [c], Florencia Marchini [c], Jean-Noël Chotard [a,b], François Fauth [f], Emmanuelle Suard [g], François Rabuel [a,b], Houssny Bouyanfif [h], Andrey D. Poletayev [i], Christopher Davies [i], Benjamin Zelin [i], M. Saiful Islam [i], Virginie Viallet [a,b], Christian Masquelier [a,b,j,*]

[a] Laboratoire de Réactivité et de Chimie des Solides, UMR CNRS 7314, Université de Picardie Jules Verne, Cedex 1, 80039, Amiens, France
[b] RS2E, Réseau Français sur le Stockage Electrochimique de l'Energie, FRCNRS 3459, Cedex 1, F80039, Amiens, France
[c] Umicore, 31 Rue du marais, Brussels, BE-100, Belgium
[d] Storage of Electrochemical Energy, Department of Radiation Science and Technology, Faculty of Applied Sciences, Delft University of Technology, 2629 JB Delft, the Netherlands
[e] CNRS, Université d'Orléans, CEMHTI UPR3079, 1D avenue de la recherche scientifique, Cedex, F45071, Orléans, France
[f] CELLS-ALBA Synchrotron, Cerdanyola del Vallés, E-08290, Barcelona, Spain
[g] Institut Laue-Langevin (ILL), BP 156, 71 Avenue des Martyrs, 38042 Grenoble, France
[h] Laboratoire de Physique de la Matière Condensée (LPMC), UR 2081, Université de Picardie Jules Verne, Amiens 80039, France
[i] Department of Materials, University of Oxford, Oxford OX1 3PH, UK
[j] Institut Universitaire de France, 103 boulevard Saint-Michel, 75005 Paris, France

HIGHLIGHTS

- A new compositional range of Argyrodite ionic conductors has been discovered.
- The $Li_{5.4}PS_{4.4}BrCl_{0.6}$ composition achieves an ionic conductivity of 10 mS/cm, at RT.
- Superior air stability compared to conventional lithium argyrodites is achieved.
- Well-performing all solid-state batteries were built.

ARTICLE INFO

Keywords:
Solid electrolytes
Ionic conductivity
Structure-transport correlations
Solid state batteries
CCD

ABSTRACT

Halide-enriched lithium argyrodite superionic conductors are considered as promising candidates for all-solid-state batteries due to their soft structure and high ionic conductivity. Challenges remain, including chemical instability and incompatibility with anode materials, and in addition a deeper understanding of the fundamental aspects of ionic transport and performance is required. In this study, we investigated two argyrodite mixed-halide series of compositions, $Li_{6-x}PS_{5-x}BrCl_x$ and $Li_{5.5}PS_{4.5}Br_{1.5-x}Cl_x$. By employing a range of techniques including X-ray diffraction (XRD), neutron diffraction, nuclear magnetic resonance (NMR) spectroscopy, electrochemical impedance spectroscopy and machine learning based molecular dynamics, we found that increasing the halide substitution enhances ionic conductivity. Notably, the $Li_{5.4}PS_{4.4}BrCl_{0.6}$ composition achieves an ionic conductivity of 10 mS/cm, demonstrates superior air stability compared to conventional lithium argyrodites and allows for the fabrication of well-performing all solid-state batteries. Our results reveal that in lithium-poor compositions the lithium environments in the 4a and 4d cages become more alike, facilitating fast long-range lithium-ion transport. This work paves the way for the development of air-stable, high-conductivity sulfide electrolytes, advancing the practical implementation of solid-state batteries.

This article is part of a special issue entitled: In memory of Professor Bruno Scrosati published in Journal of Power Sources.

* Corresponding author. Laboratoire de Réactivité et de Chimie des Solides, UMR CNRS 7314, Université de Picardie Jules Verne, Cedex 1, 80039 Amiens, France
E-mail address: christian.masquelier@u-picardie.fr (C. Masquelier).

https://doi.org/10.1016/j.jpowsour.2025.238175
Received 3 June 2025; Received in revised form 4 August 2025; Accepted 17 August 2025
Available online 23 August 2025

1. Introduction

Lithium-ion batteries (LIBs) are widely used in portable electronics and electric vehicles due to their high electrochemical performance and long cycle life. However, the liquid electrolytes in LIBs present safety risks, such as flammability, leakage, and lithium dendrite formation, which can reduce battery lifespan [1–3]. Solid-state batteries (SSBs), which use solid electrolytes, offer a safer alternative while enabling higher energy densities and broader operational temperatures [4,5]. Various lithium-ion solid electrolytes, including oxides, phosphates, halides, and argyrodites, have been studied [6,7]. Oxide-based electrolytes generally have a wide electrochemical window and good stability in air. However, their ionic conductivity at room temperature is usually low, as seen in $Li_{6.75}La_3Zr_{1.75}Ta_{0.25}O_{12}$ (LLZTO, 0.9 mS cm^{-1}). Additionally, their synthesis often involves complex procedures, including high-temperature sintering. On the other hand, halide electrolytes present several benefits, such as high ionic conductivity at room temperature and excellent oxidation stability, demonstrated by materials such as Li_3InCl_6 (1.49 mS cm^{-1}) [8], $Li_2Sc_{2/3}Cl_4$(1.5 mS cm^{-1}) [8], and $LiTaCl_6$ (10 mS cm^{-1}) [9]. However, the high cost of raw materials including $ScCl_3$, $InCl_3$, and $TaCl_5$ limits their potential for large-scale use [10].

Lithium argyrodites have attracted significant interest due to their high ionic conductivity, low cost, good ductility, excellent electrode stability, and simple synthesis process. The most common form, Li_6PS_5X (where halide X = Cl, Br, I), achieves ionic conductivities ranging from 0.001 to 4 mS/cm [11–17]. By adjusting the halide composition, particularly increasing the Cl content, the disorder between S^{2-}/X^- at the 4a/4d sites enhances ionic conductivity [18–20]. Computer simulation studies suggest that maximum conductivity is achieved when Cl^- occupies 75 % of the 4d site [21,22]. Substituting P with aliovalent elements (e.g., Ge or Si) further increases Li^+ substructure disorder, significantly boosting conductivity, as seen in compounds like $Li_{6.6}P_{0.4}Ge_{0.6}S_5I$ (5.4 mS/cm) and $Li_{6.6}Si_{0.6}Sb_{0.4}S_5I$ (14.8 mS cm^{-1}) [23–25]. However, the high cost and instability of Ge- or Sb-containing argyrodites with lithium metal anodes and high-voltage cathodes limit their use [26].

Another widely explored strategy to enhance ionic conductivity in argyrodite $Li_6(PS_4)(S)(X)$ is substituting the "free" sulfur with halogen atoms. This substitution not only increases the concentration of Li^+ vacancies but also introduces greater S^{2-}/X^- site disorder, both of which synergistically improve ionic mobility. Notably, halide-rich argyrodites with the composition $Li_{6-y}PS_{5-y}X_y$ (y > 1) demonstrate substantially higher ionic conductivity (up to 24 mS cm^{-1}) compared to conventional Li_6PS_5X counterparts [27,28]. Nazar et al. [29] investigated chloride-rich $Li_{6-x}PS_{5-x}Cl_{1+x}$ ($x \leq 0.5$) compositions of high conductivity of 9 mS cm^{-1} (12 mS cm^{-1} upon sintering) and a lower activation energy of 0.29 eV for $Li_{5.5}PS_{4.5}Cl_{1.5}$. Following this work, Feng et al. [30] further increased Cl^- content and found a solubility limit up to x = 0.7 and reported 17 mS cm^{-1} at 25°C and low activation energy of 0.22 eV for $Li_{5.3}PS_{4.3}Cl_{1.7}$. Janek et al. [31] have shown that $Li_{5.5}PS_{4.5}Cl_{1.5}$ performs better in ASSBs when compared with Li_6PS_5Cl. Bromine-rich compositions $Li_{6-x}PS_{5-x}Br_{1+x}$ ($x \leq 0.7$) were recently investigated by Wang et al. [32] who reported a high ionic conductivity of 11 mS cm^{-1} and a low activation energy of 0.18 eV. Recently, Wagemaker et al. [33] conducted a neutron diffraction study of the same compositions and showed that with increasing Br^- content in the structure, an expansion of the dimensions of the Li^+ cages occurs, which enables an alternative jump route (T5-T4-T5) for Li^+ with a lower migration energy barrier [33]. In this case the ionic conductivity increases from 0.78 to 6.2 mS cm^{-1} from Li_6PS_5Br to $Li_{5.5}PS_{4.5}Br_{1.5}$ along with the increase in activation energy 0.36–0.40 eV [33].

A contrasting difference exists between two reports by Wang et al. [32] and Wagemaker et al. [33], where with increasing Br^- content, the former reports the increase in lattice constant and decrease in activation energy whereas the latter reports the opposite trend. Although Br^-(196 p.m.)) is larger than S^{2-} (184 p.m.), and one might expect the lattice to always expand when Br^- replaces S^{2-}, this is not always the case. In slow-cooled samples, the lattice parameter **decreases** with more Br^-, while in fast-cooled (quenched) samples, it **increases**. Wagemaker et al. suggest that in slow-cooled samples, the Br^- content at the 4a site stays almost the same, so the lattice shrinkage might be due to more Li^+ vacancies or changes in Li^+ distribution. Furthermore Zhang et al. [34] reported the synthesis of iodine-rich $Li_{6-x}PS_{5-x}I_{1+x}$ by ball milling which resulted in the improvement of ionic conductivity from 0.15 to 0.31 mS cm^{-1} from x = 0 to 0.5. However, after annealing the halide-rich $Li_{5.5}PS_{4.5}I_{1.5}$ showed a significant impurity content, suggesting the unlikely possibility of synthesizing pure $Li_{5.5}PS_{4.5}I_{1.5}$.

Instead of a single type of halide, there exists a possibility to mix the halides to achieve an even higher degree of occupational disorder. Among Cl^-/Br^- mixing, Patel et al. [28] investigated a mixed halide composition $Li_{6-x}PS_{5-x}ClBr_x$ ($0 \leq x \leq 0.8$) and achieved a remarkably high ionic conductivity of 24 mS cm^{-1} and an unusually low activation energy of 0.15 eV. Masuda et al. [35] studied $Li_{7-x-y}(PS_4)(S_{2-x-y}Cl_xBr_y)$ compositions and showed that an ionic conductivity of 11.2 mS cm^{-1} can be achieved for $Li_{5.4}PS_{4.4}BrCl_{0.6}$ and $Li_{5.4}PS_{4.4}ClBr_{0.6}$ while $Li_{5.4}PS_{4.4}Cl_{1.6}$ and $Li_{5.4}PS_{4.4}Br_{1.6}$ showed slightly inferior ionic conductivity. This is due to the higher configurational entropy ($\Delta S_{conf} > 1.5$ R) which arises from shared occupancies by $S^{2-}/Cl^-/Br^-$ on a single crystallographic site as recently shown by Strauss et al. [36] in $Li_{5.5}PS_{4.5}Br_{1.5}Cl_x$. Among Cl^-/I^- mixed halide compositions, Yan et al. [37] synthesized $Li_{5.7-x}PS_{4.7-x}Cl_{1.3}I_x$ (x = 0 to 0.3) and achieved higher ionic conductivity and better stability against Li metal when compared to Li_6PS_5Cl. Along with improved ionic conductivity, halide-rich argyrodites also show greater moisture stability when compared to Li_6PS_5X [38]. In general, all the halide-rich compositions have shown better ionic conductivity and electrochemical properties when compared to Li_6PS_5X compositions. Hence, the majority of the aforementioned studies are devoted to detailed structural investigations and ionic conductivity measurements, but with less emphasis on performance in ASSBs in a comparative manner. In a patent application by Hu et al. [39] a wide range of halide rich compositions such as, $Li_{6-x}PS_{5-x}Cl_{1+x}$, $Li_{6-x}PS_{5-x}Br_{1+x}$, $Li_{6-x}PS_{5-x}ClBr_x$ and $Li_{6-x}PS_{5-x}ClI_x$ have already been covered. However, to the best of our knowledge there are no reports on the $Li_{6-x}PS_{5-x}BrCl_x$ and $Li_{6-x}PS_{5-x}BrI_x$ series. Although, $Li_{6-x}PS_{5-x}BrCl_x$ appears similar to $Li_{6-x}PS_{5-x}ClBr_x$, the latter shows an increase in lattice volume with increasing x, whereas we anticipate a decrease in lattice volume for $Li_{6-x}PS_{5-x}BrCl_x$. Additionally, Zeier et al. [14] have shown that having softer and more polarizable anion leads to lower activation energy, thereby in principle Br^- rich compositions would exhibit lower activation energy compared to Cl^- rich compositions. Another added advantage of halide-rich compositions is that they require a reduced amount of the high cost Li_2S precursor (50g = ~800 €, Sigma-Aldrich). For instance, $Li_{5.4}PS_{4.4}Cl_{1.6}$ can be synthesized by utilizing 10 % less amount of Li_2S when compared to Li_6PS_5Cl and hence economically more viable.

With a key aim to find synergy between ionic conductivity and activation energy in the mixed halide compositional space, we have studied several mixed-halide rich argyrodite compositions with a primary focus on a new $Li_{6-x}PS_{5-x}BrCl_x$ and $Li_{5.5}PS_{4.5}Br_{1.5-x}Cl_x$ series. All samples were synthesized by a mechanochemical method followed by annealing at 450°C. The structure and transport properties were investigated by a range of techniques including X-Ray and neutron diffraction, Raman spectroscopy, ^{31}P magic angle spinning (MAS) NMR, and electrochemical impedance spectroscopy. The moisture stability was investigated by monitoring the amount of H_2S release as a function of time in controlled conditions. To complement the experimental work and to probe atomic-scale mechanisms, we used ab initio and machine learning based molecular dynamics methods. Finally, we present the results of electronic conductivity measurements and a detailed investigation of all solid-state batteries.

2. Results and discussions

2.1. Structural changes in $Li_{6-x}PS_{5-x}BrCl_x$ with increasing Cl content

Lithium argyrodites, Li_6PS_5X (X = Cl, Br, or I), exhibit structural disorder, particularly between X^- and S^{2-} ions at the *4d* sites, which has been linked to Li-ion conductivity. Recent studies have shown that increasing halide content for X = Cl and Br enhances ionic conductivity [15,18,28,30,32,35,40]. This improvement is rationalized in several ways: (i) the substitution of divalent S^{2-} with monovalent X^- at the *4d* site could reduce the electrostatic interaction between Li ions and anions occupying the *4d* sites, (ii), the occupation of the lithium T4 site could offer an additional path for inter-*4d*-cage movement [25,33], (iii) configurational entropy and increased similarity between *4a* and *4d* cages could enable effective long-range transport [15,40]. Overall, the substitution of S with a mix of Cl and Br in the $Li_{6-x}PS_{5-x}BrCl_x$ system, and its impacts on air stability, lithium substructure, the structural framework, and ionic transport mechanisms, remain underexplored and require further investigation.

To investigate the impact of halide substitution on the structure, the $Li_{6-x}PS_{5-x}BrCl_x$ series ($0 \leq x \leq 0.8$) was synthesized using ball milling followed by heat treatment at 450°C. Structural analysis was conducted using X-ray diffraction (XRD) and neutron diffraction, with Rietveld refinements applied to examine both structural changes and Li^+ sub-structures. In this series, the Cl content was systematically increased in steps of x = 0.1, up to a maximum of x = 0.8. Representative XRD patterns for $Li_{6-x}PS_{5-x}BrCl_x$ compositions ($0 \leq x \leq 0.8$) are shown in Fig. 1a & b, revealing the argyrodite phase within the $F\bar{4}3m$ space group for compositions up to x = 0.7. The absence of impurity or precursor diffraction peaks indicates the high purity of the samples. For nominal x = 0.8, phase segregation occurred, as evidenced by the splitting of a single peak into two distinct peaks, corresponding to separate Li_6PS_5Br and Li_6PS_5Cl phases, which indicates that the solubility limit of Cl^- in the $Li_{6-x}PS_{5-x}BrCl_x$ system is x = 0.7. This solubility limit is consistent with other halide-rich compositions, such as $Li_{6-x}PS_{5-x}Cl_{1+x}$, $Li_{6-x}PS_{5-x}Br_{1+x}$ and $Li_{6-x}PS_{5-x}ClBr_x$, reported in the literature [18,28].

As the Cl content increases up to x = 0.7, the XRD peaks' positions shift to higher 2θ values, as illustrated in Fig. 1b, which signifies a decrease of the lattice parameter, *a*, of the cubic unit cell. Decrease in the lattice constant may be primarily due to the Li^+ vacancies created upon Cl^- incorporation and increased disorder on the *4a* and *4d* sites, similar to simpler compositions [20]. Simulation results (detailed below) further confine this effect to a compression of the lithium cages around the *4a* sites, whereas the geometries of the lithium *4d* cages remain virtually unchanged. The lattice parameter obtained from profile matching of the XRD patterns linearly decreases from 9.992(1) to 9.908 (1) Å as shown in Fig. 1c, supporting x = 0.7 as the solubility limit of Cl^- in the system. This finding aligns with other halide-rich compositions ($Li_{6-x}PS_{5-x}Cl_{1+x}$, $Li_{6-x}PS_{5-x}Br_{1+x}$ and $Li_{6-x}PS_{5-x}ClBr_x$) and suggests that a nominal Li^+ content of 5.3 in the composition is necessary to stabilize the argyrodite phase.

High-resolution neutron powder diffraction (NPD) measurements were conducted to study the lithium substructure and the occupancies of Cl and S at the *4a* and *4d* sites. The measurements were collected at room

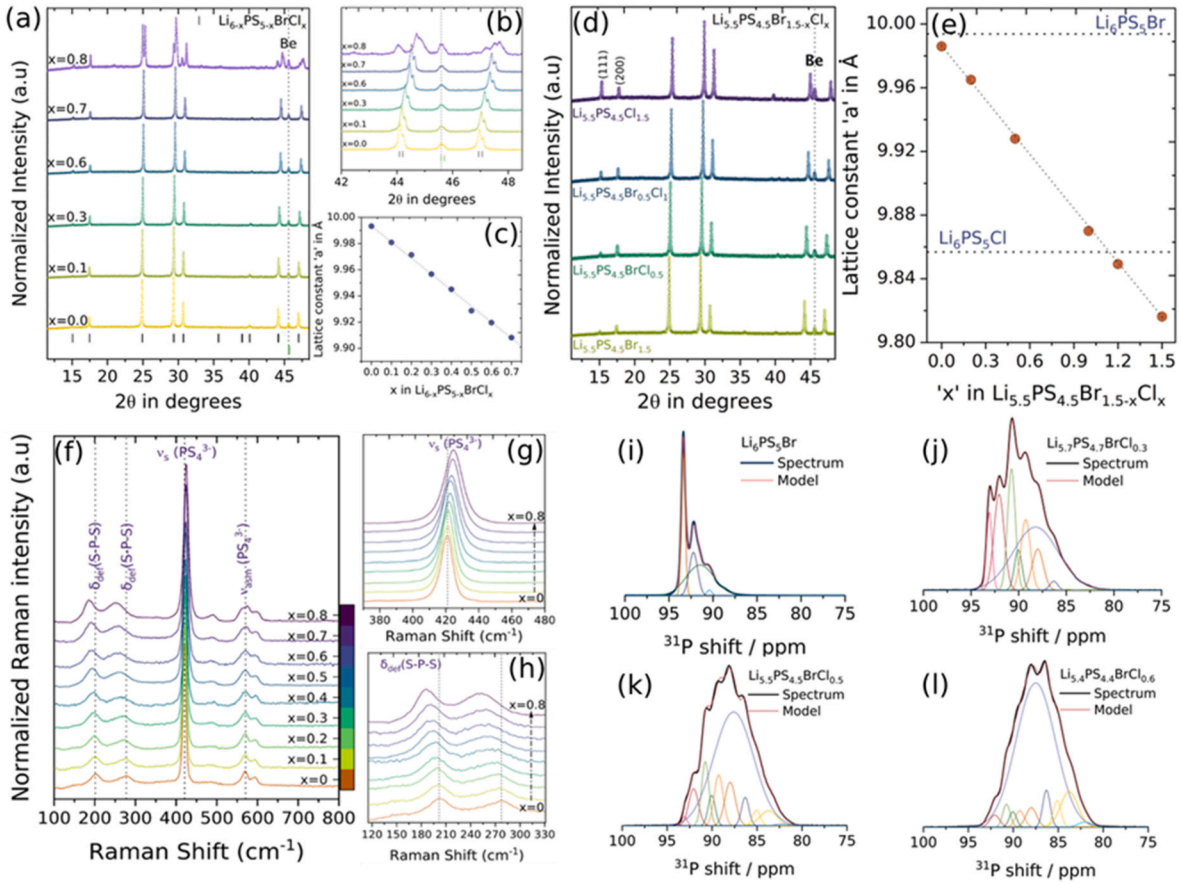

Fig. 1. (a) and (b) XRD patterns of $Li_{6-x}PS_{5-x}BrCl_x$ with increasing x values. (c) Variation of lattice parameter as a function of x in $Li_{6-x}PS_{5-x}BrCl_x$. (d) XRD patterns of $Li_{5.5}PS_{4.5}Br_{1.5-x}Cl_x$ with increasing x and (e) variation of lattice constant 'a' with increasing x in $Li_{5.5}PS_{4.5}Br_{1.5-x}Cl_x$. The lattice constants of Li_6PS_5Br and Li_6PS_5Cl are also shown for comparison. (f) Raman spectra of $Li_{6-x}PS_{5-x}BrCl_x$ with increasing x. (g) and (h) show the shift of the Raman peaks corresponding to symmetric stretches and deformation mode of S-P-S of PS_4 units respectively. (i) to (l) 31P MAS NMR spectrum of Li6PS5Br, Li5.7PS4.7BrCl0.3, Li5.5PS4.5BrCl0.5 and Li5.4PS4.4BrCl0.6 respectively, obtained at 17.4 T (10 kHz MAS).

temperature from selected samples of $Li_{6-x}PS_{5-x}BrCl_x$, with x = 0, 0.3, 0.5, and 0.6. A representative diffraction pattern for $Li_{5.4}PS_{4.4}BrCl_{0.6}$ along with the corresponding Rietveld refinement profile is depicted in Fig. 2a (other plots are shown in Supplementary Information Fig. S1). The calculated lattice constants from XRD and NPD are in excellent agreement with each other and the obtained structure is shown in Fig. 2b, In the mixed halide argyrodites, the three anions (S^{2-}, Cl^-, and Br^-) are distributed over two distinct crystallographic sites (*4a* and *4d*). Due to the complexity of having three atoms occupying the same positions, we constrained the total occupancy of both the *4a* and *4d* sites to equal 1 for each. By refining all the occupancies together under this constraint, we achieved the best possible fit for the data. Structural data are tabulated in supplementary information.

The obtained $S^{2-}/Cl^-/Br^-$ occupancy % on the 4*a* and 4*d* site for x = 0, 0.3, 0.5 and 0.6 are shown in Fig. 2c and d. At x = 0 (Li_6PS_5Br), the Br^- occupancies over the 4*a* and 4*d* sites are 81 % and 19 % respectively. Although Br^- prefers to occupy the larger 4*a* site in Li_6PS_5Br, with increasing x, the Br^- occupancy on the 4*d* site increases from 19 % to 30 % between x = 0 to x = 0.6. This increased Br^- occupancy % on the 4*d* site (increased site-disorder) is beneficial to obtain a higher ionic conductivity, as already identified by Zeier et al. [18,20,33,41] Similarly, as the chloride content increases with x, the Cl^- occupancy on the 4d site increases from 0 % to 42 % between x = 0 and x = 0.5. At x = 0.6, the 4d site is occupied by 40 % Br^-, 36 % Cl^-, and 24 % S^{2-}. The randomness in the halogen distribution in the crystal structure also affects the Li substructure. For the mixed halide argyrodites, 4 different Li positions, namely T5 (Wyckoff 48*h*), T4 (Wyckoff 16*e*), T5a (Wyckoff 24*g*) and T2 (Wyckoff 48*h*) shown in Fig. S2, were identified by Masuda et al. [35] In our case, for x = 0 and 0.6 three Li positions, namely T2, T4, and T5, were identified as yielding meaningful B_{iso} and occupancy values. For all of our compositions, without constraining the Li occupancies, the refined Li occupancies were always less than targeted values. In this series, as the chloride content increases, the occupancy of the T4 site increases. Since T4 sites are approximately as close to *4a* sites as T2 sites are (although along differing crystallographic directions), their population signifies an increasingly uniform lithium distribution throughout the material and increasing similarity between *4a* lithium cages and *4d* lithium cages. We return to this point below when discussing computational results. Additionally, with increasing Cl content, the overall lithium content decreases and site disorder increases, both of which can contribute to shrinking the lattice parameter.

As a next step, we maintained the nominal Li content constant ($Li_{5.5}$) and varied the halide distribution starting from Br^- rich to Cl^- rich composition in the series, $Li_{5.5}PS_{4.5}Br_{1.5-x}Cl_x$ with $0 \leq x \leq 1.5$. The XRD patterns of the representative samples in $Li_{5.5}PS_{4.5}Br_{1.5-x}Cl_x$ are depicted in Fig. 1d. All the diffraction peaks can be assigned to the argyrodite phase in the space group: $F\bar{4}3m$. The lattice parameter 'a' derived from the profile matching as a function of varying x in $Li_{5.5}PS_{4.5}Br_{1.5-x}Cl_x$ are shown in Fig. 1e and the lattice constants of Li_6PS_5Br and Li_6PS_5Cl are also shown for the comparison. The linear decrease in lattice constant across the entire compositional range substantiates the solid solution behaviour, primarily attributed to the lower ionic radii of Cl^- relative to Br^-, while maintaining the same nominal levels of lithium, sulfur, and phosphorus. Notably, the lattice constant of $Li_{5.5}PS_{4.5}Br_{1.5}$ is lower than that of Li_6PS_5Br, which is an observation contradictory to that of Hu et al. [32] but in agreement with the recent report from Wagemaker et al. [33]. In the case of $Li_{5.5}PS_{4.5}Br_{1.5}$, in contrast to the expected increase in lattice constant arising from the larger Br^- ions, the concomitant decrease in the nominal Li content and increase in the anion site disorder exert a superseding effect on lattice shrinkage, thereby resulting in a lower lattice constant compared to Li_6PS_5Br [33].

Raman spectroscopy measurements were performed to confirm the sample purity and provide hints on structural changes resulting from the increasing Cl^- in $Li_{6-x}PS_{5-x}BrCl_x$. The Raman spectra of $Li_{6-x}PS_{5-x}BrCl_x$ ($0 \leq x \leq 0.8$), shown in Fig. 1f contain four prominent peaks at around 204, 276, 421, and 571 cm^{-1} (for x = 0) attributed to the different vibrational modes of PS_4^{3-} tetrahedra. With increasing 'x'

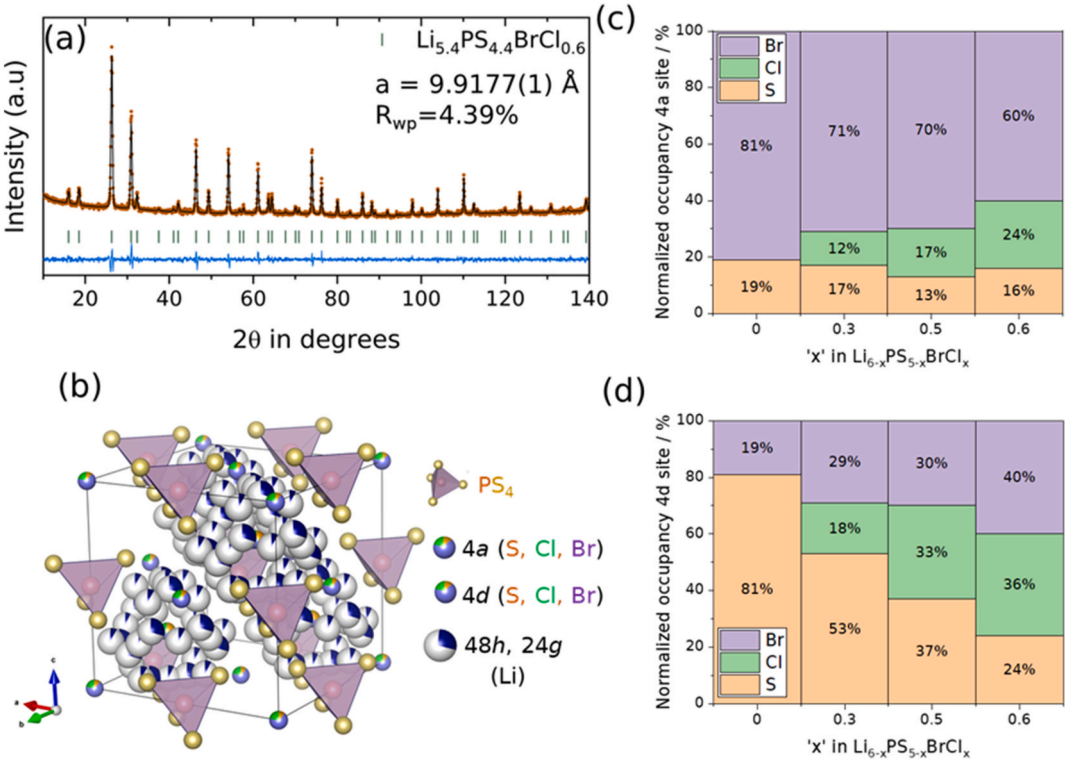

Fig. 2. (a) Neutron powder diffraction pattern and Rietveld refinement profile for $Li_{5.4}PS_{4.4}BrCl_{0.6}$. (b) crystal structure of $Li_{5.4}PS_{4.4}BrCl_{0.6}$ with the different Wyckoff positions and elemental constituents indicated in the legend to the right. (c) and (d) The normalized occupancies of the *4d* and *4a* Wyckoff positions depicted in the panels.

the Raman peak corresponding to the symmetric stretches of the PS_4 units (Fig. 1g) is broadened and is gradually shifted to higher wavenumbers, from 421 to 424.3 cm^{-1} for x = 0.0 to 0.7. This is most likely due to the decreasing unit-cell and to the altered bond lengths due to random distribution of Br^- and Cl^- in the structure. However, the Raman peak at 571 cm^{-1} corresponding to the asymmetric stretching mode remains mostly unaltered except for x = 0.8, which is due to the phase segregation, as observed from XRD. Additionally, a small peak around 470 cm^{-1} is observed corresponding to S-S stretching and bending modes [42]. Notably, the two peaks at 204 and 276 cm^{-1} corresponding to the deformation modes of S-P-S in PS_4^{3-} shift to lower wavenumbers upon increasing the amount of Cl as shown in Fig. 1h. The opposite trend in the phonon shift (hardening for the 421 cm^{-1} phonon and softening for the 204 - 276 cm^{-1} doublet) is indeed reminiscent of melting behavior (weaker influence of lattice environment/Li sublattice on internal PS_4 frequencies) as previously observed in Na_3PS_4 and isolated PS_4 phonon frequencies measured in aqueous solution [43,44].

To gain a deeper understanding of the P environment in this series of new compositions, we conducted ^{31}P MAS NMR measurement of Li_6PS_5Br, $Li_{5.7}PS_{4.7}BrCl_{0.3}$, $Li_{5.5}PS_{4.5}BrCl_{0.5}$ and $Li_{5.4}PS_{4.4}BrCl_{0.6}$ as shown in Fig. 1i–l. The ^{31}P NMR spectra of the four samples are centered in the range 80–95 ppm, as expected from literature for PS_4^{3-} tetrahedra [45,46]. The multiple components of each spectrum arise from the superposition of slightly differing local environments for the phosphorus atoms, which we assign to the 4 s anionic neighbours that occupy the 4d sites around the PS_4^{3-} tetrahedron (P-4d distance = a/2).

In the Li_6PS_5Br structure, due to the mixed occupation Wyckoff 4*d* site occupation by Br^-/S^{2-}, five distinct local ^{31}P environments are expected, corresponding to 4S, 3SBr, 2S2Br, 1S3Br and 4Br on the Wyckoff 4*d* positions. The ^{31}P NMR spectrum of Li_6PS_5Br was fitted into a set of 3 relatively narrow Gaussian-shaped functions centered at 93.3 ppm, 92.2 ppm, and 90.3 ppm, assigned previously to PS_4^{3-} units with configurations 4S, 3S1Br and 2S2Br on the 4 neighbouring 4d sites (no 4Br environments). Contrary to recent reports for Li_6PS_5Br [32] or for the endmembers $Li_{5.5}PS_{4.5}Cl_{1.5}$ and $Li_{5.5}PS_{4.5}Br_{1.5}$ [36] or $Li_{6-x}PS_{5-x}Br_{1+x}$ [15], an additional extremely broad Gaussian-shaped peak centered at 91.3 ppm was necessary for a reasonable fit, which we tentatively assign to a PS_4^{3-} environment with a less well-defined second coordination sphere, possibly due to increased mobility of Li next to the PS_4^{3-} units, to a slight tilting of the PS_4^{3-} orientation, or to an additional effect of third anionic neighbours on the 4a sites (only slightly further away: P-4a distance = a $\sqrt{3}/4$) [47]. In contrast, for $Li_{6-x}PS_{5-x}BrCl_x$, where Wyckoff 4*d* position is potentially occupied by $Br^-/S^{2-}/Cl^-$, the complexity of the potential phosphorus local environments arises, with the potential for 15 distinct local arrangements of the neighbouring second anionic neighbours, including 4S, 3S-1Br, 3S-1Cl, 2S-1Cl-1Br, 2S-2Cl, 2S-2Br, 1S-1Cl-2Br, and so forth. Experimentally with increasing Cl^- content, the relative proportion of the peaks at lower ppm increase, in agreement with previous reports [15,36,48].

Owing to the difficulty of under-constrained fitting of the NMR data with 15 Gaussian-shaped functions, we decided to constrain the fit to the minimal amount (10) of relatively narrow Gaussian-shaped functions that enabled a reasonable fit of all the data while keeping identical the positions and widths across the series of samples. The 10 resulting ^{31}P environments in the fit for $Li_{5.7}PS_{4.7}BrCl_{0.3}$, $Li_{5.5}PS_{4.5}BrCl_{0.5}$ and $Li_{5.4}PS_{4.4}BrCl_{0.6}$ are centered between 93.09 ppm and 82.08 ppm, with varying relative areas (Table 1). As for Li_6PS_5Br, an additional broad Gaussian shaped function (peak 11) was necessary to obtain good fits. The shift and width of peak 11 had to vary across the series to ensure correct fitting. The increase of relative integral of peak 11 (Table 1) with increasing Cl^- content may indicate towards an increased Li mobility or increased disorder in the PS_4^{3-} units tilting.

By considering the multinomial distribution of S, Br, Cl and the 4*d* occupancies (x1; x2, x3) obtained from neutron diffraction, the relative populations of the 15 expected environments can be predicted by using the probability function below, with populations tabulated in Table S5 in the case of independent populations

$$P(S=x_1, Br=x_2, Cl=x_3) = \frac{4!}{x_1!\cdot x_2!\cdot x_3!} S^{x_1}\cdot Br^{x_2}\cdot Cl^{x_3}$$

A good agreement of this probability function with the areas of the individual peaks of the fit would indicate that the probability of one type of atom occupying one of the 4d sites does not affect the probability of other atoms occupying the remaining three 4d sites. As the fit for each composition contains fewer environments than expected, it was not possible to assign directly each peak to a particular configuration of S, Br, and Cl on 4*d* site. Still, we tentatively added the calculated probabilities of the arrangement containing the same total number of (Br + Cl), assuming that they are the main cause for displacing the 31P peaks to lower shifts. A weak trend towards decreasing shift with decreasing S content (increasing Br + Cl content) of the neighbouring *4d* sites is indeed reproduced in first-principles calculations (Supplementary Information).

Our approach reduces the number of arrangements for the 4d sites around the PS_4^{3-} units down to six (namely 4Cl/4Br, 4X,1S2X, 2S2X, 3S1X, 4S with X = Br or Cl, detailed list in Table S5). The multinomial probabilities for random arrangement are plotted in grey in Fig. S4. We managed to add peaks together from the experimental fit for $Li_{5.7}PS_{4.7}BrCl_{0.3}$ to reduce it to 6 environments with areas in reasonable agreement with the calculated probabilities for a random arrangement (multinomial), as plotted in orange in Fig. S4a. However, this treatment of the experimental fits provided discrepancies for $Li_{5.5}PS_{4.5}BrCl_{0.5}$ and $Li_{5.4}PS_{4.4}BrCl_{0.6}$. These discrepancies between the multinomial distribution and the experimental fit may be due to a non-random arrangement, for example if the presence of Cl restricts the probability of Br being in the same coordination shell. This would not change the average probability as measured from neutron diffraction, but would modify the

Table 1
Characteristics of the Gaussian peaks used for the ^{31}P NMR fits for $Li_{6-x}PS_{5-x}BrCl_x$ Areas are obtained by integration of the isotropic peak, neglecting differences in chemical shift anisotropy.

Peak #	Shift/ppm			Width/ppm			Area/%		
Composition	x = 0.3	x = 0.5	x = 0.6	x = 0.3	x = 0.5	x = 0.6	x = 0.3	x = 0.5	x = 0.6
1	93.09	93.09	93.09	0.68	0.68	0.68	6.4	0.67	0
2	92.07	92.07	92.07	1.27	1.27	1.27	14.7	5.02	1.5
3	90.76	90.76	90.76	0.96	0.96	0.96	14.08	6.58	2.28
4	90.05	90.05	90.05	0.94	0.94	0.94	4.58	3.05	1.53
5	89.27	89.27	89.27	1.17	1.17	1.17	9.96	6.3	2.24
6	88	88	88	1.39	1.39	1.39	6.95	6.44	3.08
7	86.32	86.32	86.32	0.96	0.96	0.96	1.02	2.91	3.39
8	85.07	85.07	85.07	1.02	1.02	1.02	0.08	1.69	2.47
9	83.72	83.72	83.72	2.25	2.25	2.25	0	3.6	6.79
10	82.08	82.08	82.08	1.79	1.79	1.79	0.1	0.36	0.62
11	**88.21**	**87.61**	**87.41**	**5.59**	**5.22**	**5.27**	**42.14**	**63.39**	**76.09**

relative intensities in the NMR spectrum. Alternatively, changes in lithium mobility or in tilting of the PS_4^{3-} with varying lithium and chlorine contents may be responsible for changing peak widths, which we did not allow in the present analysis.

Although similar compositions were studied by Hu et al.[30,3248], Wagemaker et al. [15] and Strauss et al. [36], yet a comprehensive understanding of the spectra of the mixed halide compositions still needs to be pursued. A more robust simulation of ^{31}P spectra would require averaging configurations over the timescale of the Larmor frequency of the measurement [49], which is left to further study.

2.2. Ionic transport within $Li_{6-x}PS_{5-x}BrCl_x$ and $Li_{5.5}PS_{4.5}Br_{1.5-x}Cl_x$

To assess the ion transport properties, temperature-dependent impedance spectroscopy measurements were performed in the temperature range of −20 °C–50 °C. All the measurements were carried out on

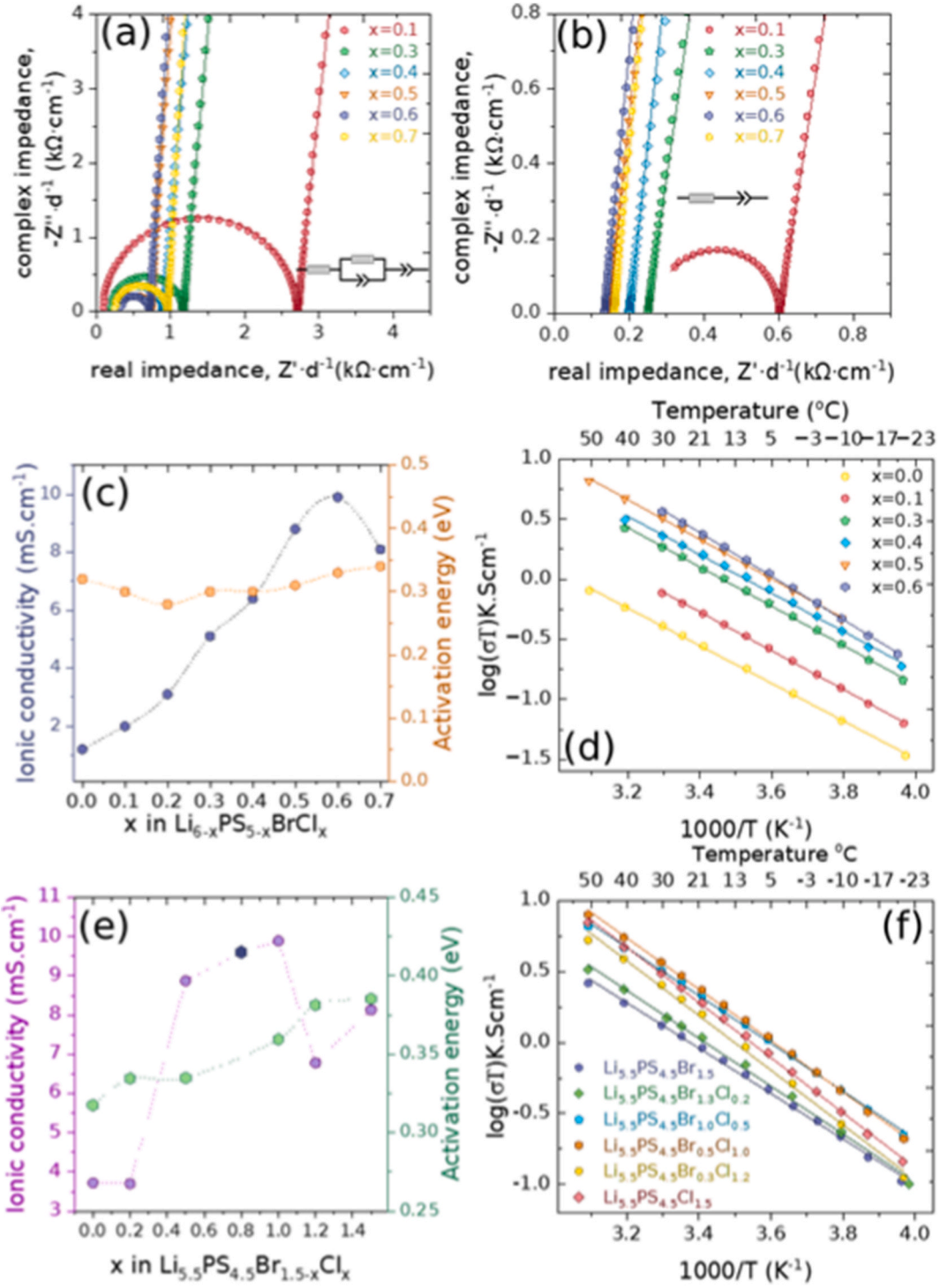

Fig. 3. Nyquist plots of $Li_{6-x}PS_{5-x}BrCl_x$ at (a) −10°C and (b) 25°C. The Inset shows the equivalent circuit model used to fit the data. (c) Variation of ionic conductivity and activation energy as a function of increasing x in $Li_{6-x}PS_{5-x}BrCl_x$ at 298 K (d) Arrhenius plots of $Li_{6-x}PS_{5-x}BrCl_x$. (e) Variation of ionic conductivity measured at 298 K and activation energy as a function of increasing x in $Li_{5.5}PS_{4.5}Br_{1.5-x}Cl_x$. (f) Arrhenius plots of $Li_{5.5}PS_{4.5}Br_{1.5-x}Cl_x$.

pellets of 10 mm diameter and about 1.25–1.3 mm thickness which were pressed under 5 Tons, resulting in density of 85–87 %. Thin indium foils of thickness ~60 μm and 10 mm diameter were used as ion-blocking electrodes in all the cases. Normalized Nyquist plots of $Li_{6-x}PS_{5-x}BrCl_x$ at −10°C and 25°C are represented in Fig. 3a and b respectively. For the Nyquist plots at −10 °C (Fig. 3a), a semicircle representing contributions from both the bulk and grain boundaries was observed. The data was fitted with an equivalent circuit model (R_c-(R|CPE)-CPE), where R_c represents the resistance from contacts and wires, R/CPE corresponds to the sample contribution, and CPE represents the blocking electrodes. At 25 °C, all samples except the one with x = 0.1 showed capacitive blocking behaviour of the electrodes, which is commonly observed in materials with low resistance or very high ionic conductivity [25,50]. Consequently, all data were fitted with an equivalent circuit containing a resistor in series with a constant phase element (R-CPE), where R represents the total resistance (including both bulk and grain-boundary resistance), and the CPE represents the blocking electrodes. By visual inspection, it is evident that resistance decreases as x increases in $Li_{6-x}PS_{5-x}BrCl_x$, with the lowest resistance observed at x = 0.6 for $Li_{5.4}PS_{4.4}BrCl_{0.6}$. Arrhenius plots for compositions with x values from 0.0 to 0.6 are shown in Fig. 3c that shows the temperature-dependent ionic conductivity, which increases with temperature, following a linear trend consistent with an Arrhenius behaviour. Ionic conductivity increases gradually from 1.2 mS cm^{-1} for x = 0 to 9.8 mS cm^{-1} for x = 0.6 within the $Li_{6-x}PS_{5-x}BrCl_x$ series. This was confirmed by additional measurements for same composition by making pellets of thickness 0.13, 0.25 and 0.31 cm and the Nyquist plots at 25 °C and −10 °C are shown in Fig. S3a and S3b respectively. All the data were fitted with an equivalent circuit (R-CPE) and the ionic conductivity at 25 °C for three pellets with (t) = 0.13, 0.25 and 0.31 cm are 9.8, 10.2 and 10.4 mS cm^{-1} respectively. At −10 °C, a single semicircle is observed comprising of bulk and grain boundary contributions. Calculated ionic conductivities at −10 °C are 1.8, 1.9 and 2.0 mS cm^{-1}. All three values are well within the error limit, and validates our good measurement protocol and measured ionic conductivity values. Further increase in x to 0.7 leads to minor decrease in ionic conductivity to 8 mS cm^{-1}. The activation energies, calculated from the linear fit of the Arrhenius plot, slightly increase from 0.32 to 0.34 eV from x = 0 to 0.6. Notably, even at −10°C $Li_{5.4}PS_{4.4}BrCl_{0.6}$ shows a high ionic conductivity of 2 mS cm^{-1}. Enhanced ionic conductivity can be mainly attributed to the higher degree of disorder of Cl^-, Br^- and S^{2-} on the 4*a* and 4*d* sites and increased similarity of the *4a* and *4d* cages.

We further investigated Li-deficient argyrodite compositions of same Li nominal content (5.5) by changing the Br and Cl ratio. The variations of the ionic conductivity and of the activation energy as a function of increasing 'x' from 0 to 1.5 in $Li_{5.5}PS_{4.5}Br_{1.5-x}Cl_x$ are depicted in Fig. 3e and corresponding Arrhenius plots are shown in Fig. 3f. The ionic conductivity ranges from 3.7 to 9.8 mS cm^{-1} from $Li_{5.5}PS_{4.5}Br_{1.5}$ (x = 0) to $Li_{5.5}PS_{4.5}Br_{0.5}Cl$ (x = 1). Notably, when the Br and Cl mixing is maximum ($ClBr_{0.5}$ and $BrCl_{0.5}$), the ionic conductivity is higher compared to the end members, while the activation energy significantly increases from 0.32 to 0.39 eV when transitioning from Br-rich ($Br_{1.5}$) to Cl-rich ($Cl_{1.5}$) compositions. Comparing the two highly conductive compositions, i.e. $Li_{5.5}PS_{4.5}ClBr_{0.5}$ with $Li_{5.5}PS_{4.5}BrCl_{0.5}$, the former exhibits a higher ionic conductivity of 9.8 mS.cm^{-1}at 298K accompanied by a slightly higher activation energy of 0.36 eV. Conversely, the latter displays a marginally lower ionic conductivity of 8.9 mS cm^{-1} at 298 K but features a lower activation energy of 0.33 eV. Hence, at 273 K, both compositions exhibit identical ionic conductivities as indicated on the Arrhenius plot. To choose the best composition, the trade-off between ionic conductivity and activation energy is a critical consideration. While higher ionic conductivity is generally desirable, the impact of increased activation energy on overall performance cannot be overlooked.

2.3. Atomic-scale mechanism of conductivity improvement in $Li_{6-x}PS_{5-x}BrCl_x$

To gain atomic-scale mechanistic insights into fast lithium-ion transport, we used ab initio methods and molecular dynamics (MD) simulations based on machine learning interatomic potentials (MLIP). We simulated the structural, dynamic, and transport properties of the $Li_{6-x}PS_{5-x}BrCl_x$ composition series for x = 0, 0.3, and 0.6 to determine the mechanism of the enhancement in lithium-ion conductivity with Cl substitution. The MLIP simulation reproduced the experimental lattice parameters to better than 0.01 Å, i.e., to within about 0.1 % (Fig. 4). For further validation of our model, the simulation also reproduces all the experimental fingerprints of Raman spectra using the sulfur vibrational density of states as a proxy. Here, we only target frequencies and their shifts with composition and do not simulate intensities to avoid computing polarizabilities.

The S-P-S distortion peaks at 204 and 276 cm^{-1} are accurate to within ≤5 cm^{-1}, and their softening with Cl substitution is reproduced (compare Figs. 4 and 1). The peak at 571 cm^{-1}, by contrast, does not soften with Cl substitution, and the peak at 421 cm^{-1} instead hardens (Fig. 4). Precise agreement with experiment allowed us to interpret three more features of the vibrational spectra. First, we assigned the feature near 150 cm^{-1} to S cages (*4a* and *4d*) based on their disappearance with decreasing S content. This was only a weak feature in the experimental Raman spectra, likely due to low polarizability. Second, based on the softening of the modes at ≤100 cm^{-1}, which most likely are acoustic and phononic, we concluded that the lattice softens with Cl substitution; a more detailed analysis of PS_4 vibrations is left for future work. Third, the Br vibrations, instead harden with Cl substitution, demonstrating an opposing trend. We interpret this below but note that in Li_6PS_5Br the Br occupies predominantly the *4a* site, which can be expected to be soft. Finally, the simulation also reproduces the increasing trend in ionic conductivities with Cl substitution at 323 K, although it overestimates their absolute magnitudes. The agreement at x = 0.6 is within a factor of 2.3x, and at x = 0.3 within a factor of 3.0x. We note that in lieu of simulating diffusivity at elevated temperatures (500 K and above) and relying on Arrhenius extrapolations or assuming a unity Haven ratio, we benchmarked directly to experimental values using long-duration simulations and ascertaining that the dispersive Jonscher regime (power-law increase of conductivity with increasing a.c. frequency) is surpassed.

We then investigated the origin of increased conductivities with Cl substitution by examining the pairwise radial distribution functions (RDF, *g(r)*) between cage anions and lithium as a proxy for cage structure following the approach by Morgan [51] but dis-aggregating cage structure by anion and cage type. With increasing x in $Li_{6-x}PS_{5-x}BrCl_x$, the *4d* cages remain unchanged (Fig. 4, orange); this can be further seen in the corresponding coordination numbers (Fig. S9). However, the *4a* cages (Fig. 4, blue) harden and compress as they accommodate the decrease in lithium stoichiometry. This occurs for both S, Cl, and Br *4a* cages (see again Fig. S9 for Cl coordination numbers). As a result, the lithium cage structure around every *4a* anion approximates that around the same anion on the *4d* site by x = 0.6: the lithium environments around the *4a* and *4d* cages become more similar with Cl substitution. Together with increasing anion disorder (Fig. 2), this helps to explain the improvement in lithium conductivity: instead of any particular cage type (*4a* or *4d*) serving as a bottleneck to transport, the landscape for lithium-ion conduction becomes effectively more uniform even if the individual hopping distances may not substantively change. A T4 site would be found at ≈3.7 Å from *4d* anions, but these are not pronounced in simulation. However, the experimental identification of T4 occupancy similarly serves to make the *4a* cages more akin to the well-defined *4d* cages.

2.4. Critical current density tests (CCD)

Although there is no direct correlation between ionic conductivity

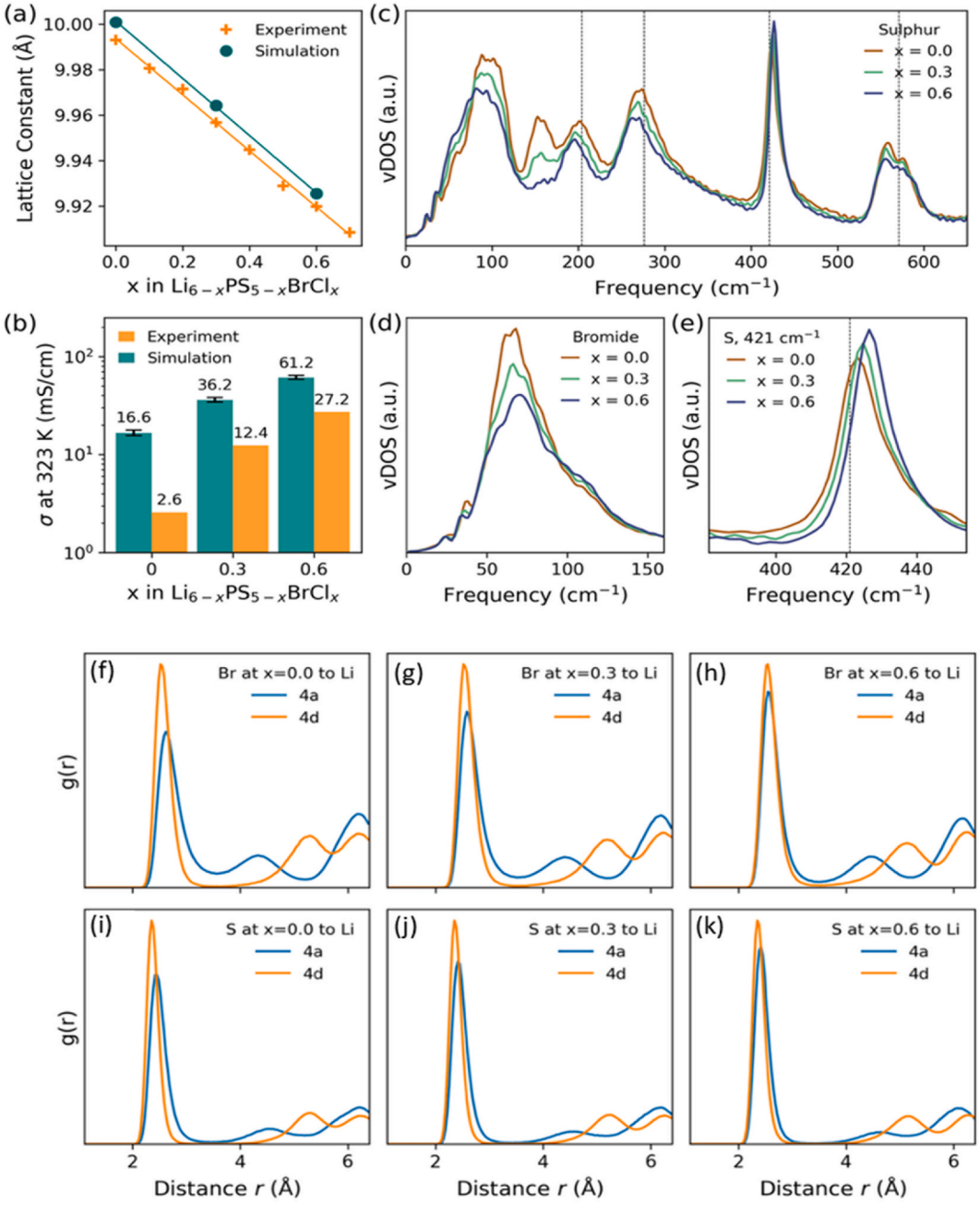

Fig. 4. Simulated structure, conductivity, and vibrational dynamics of $Li_{6-x}PS_{5-x}BrCl_x$. (a) Lattice constants from simulation (green) reproduce experiment to within 0.01 Å; experimental values from Fig. 1. (b) Li-ion conductivity simulated at 323 K reproduces the experimental trend with composition. (c) S vibrational density of states (vDOS); vertical guidelines are Raman peaks from Fig. 1. (d) Br vDOS shows broadening and hardening with Cl substitution. (e) The strong experimental S mode at 421 cm^{-1} in Li_6PS_5Br and its hardening upon Cl substitution are reproduced. Pairwise radial distribution functions between cage-center anions and Li in $Li_{6-x}PS_{5-x}BrCl_x$ from the MD simulations (f–h) Br-Li, (i–k) S-Li. Blue: *4a* cage anions, orange: *4d* cage anions. (For interpretation of the references to colour in this figure legend, the reader is referred to the Web version of this article.)

and CCD, it is commonly observed that compositions with higher conductivity tend to show higher CCD values [52–55]. To study the impact of Cl substitution on the Li dendrite suppression capability of $Li_{6-x}PS_{5-x}BrCl_x$ compositions (x = 0.0, 0.3, 0.5, 0.6), **Li | SE | Li** symmetric cells were constructed.

Li plating/stripping profiles for $Li_{6-x}PS_{5-x}BrCl_x$ (x = 0.0, 0.3, 0.6) are presented in Fig. 5a, b and 5c, respectively. For a given current density, the overpotential value decreases with increasing Cl content. In Li_6PS_5Br, the overpotential increases to 93 mV at 0.6 mA cm^{-2}, leading to a short circuit in the cell. In contrast, at the same current density, $Li_{5.7}PS_{4.7}BrCl_{0.3}$ exhibits a significantly lower overpotential of 34 mV that further decreases to 24 mV for $Li_{5.5}PS_{4.5}BrCl_{0.5}$ and $Li_{5.4}PS_{4.4}BrCl_{0.6}$. At higher current densities of >0.7 mA cm^{-2} the overpotential of $Li_{5.7}PS_{4.7}BrCl_{0.3}$ starts to increase and eventually the cell undergoes a short circuit at 0.9 mA cm^{-2}. Despite showing a lower overpotential, the CCD of $Li_{5.4}PS_{4.4}BrCl_{0.6}$ is also 0.9 mA cm^{-2}. Among the measured samples, a highest CCD of 1 mA cm^{-2} is achieved for $Li_{5.5}PS_{4.5}BrCl_{0.5}$. These observations suggest that the high ionic conductivity observed in mixed halide compositions also translates into better stability against Li metal. Since all the compositions exhibited similar particle sizes, we can speculate that mixed halide compositions may also contribute to the formation of a stable SEI layer. The SEI layer,

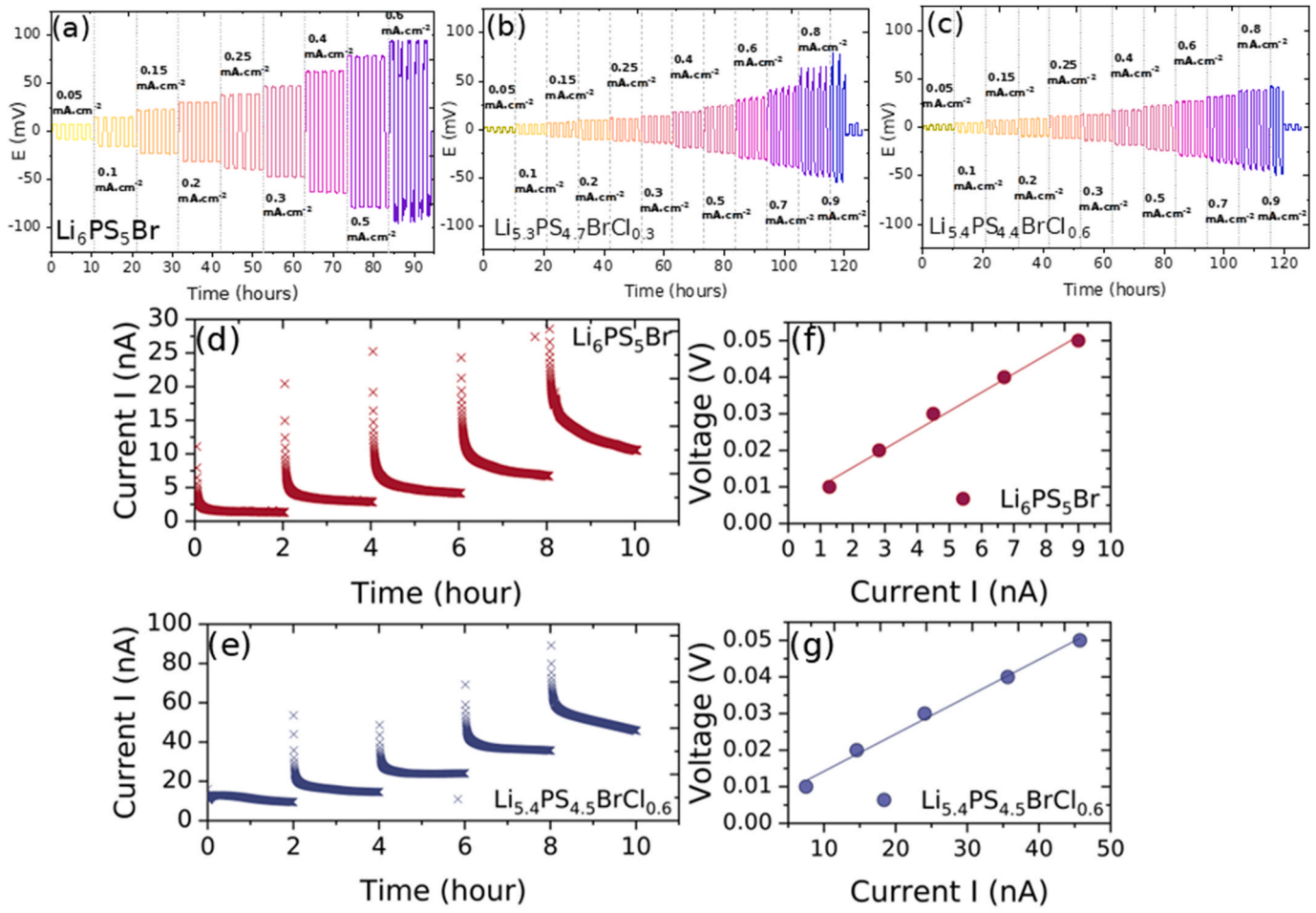

Fig. 5. Time-controlled Li plating/stripping profiles of symmetric Li | SE | Li cells under constant stack pressure of 25 MPa for (a) Li_6PS_5Br, (b) $Li_{5.7}PS_{4.7}BrCl_{0.3}$, (c) $Li_{5.5}PS_{4.5}BrCl_{0.5}$, (d) $Li_{5.4}PS_{4.4}BrCl_{0.6}$. A constant current was applied for 1 h during each charge/discharge cycle, with the current density incrementally increased from 0.05 mA.cm-2 until cell failure occurred. (d) and (f) DC polarization curves for the applied voltages of 10–50 mV for Li_6PS_5Br and $Li_{5.4}PS_{4.4}BrCl_{0.6}$ pellets respectively. (e) and (g) Typical I-V curves of Li_6PS_5Br and $Li_{5.4}PS_{4.4}BrCl_{0.6}$ plotted using current values derived from polarization curves.

likely containing both LiCl and LiBr along with Li_2S/Li_3P, probably exhibits synergistic properties. LiCl may contribute to enhanced mechanical strength and electronic passivation, while LiBr may facilitate efficient Li^+ diffusion [56,57] This improved SEI may promote homogeneous lithium deposition and robust dendrite suppression, thereby enabling a superior and stable critical current density. consequently leading to higher critical current density [58,59].

2.5. *Electronic conductivity of $Li_{5.4}PS_{4.4}BrCl_{0.6}$ in comparison to Li_6PS_5Br*

The electronic conductivity was measured by performing "classical" DC polarization experiments, for which after a small voltage applied, the resulting leakage current was measured over time. From these measurements the electronic resistance (R_e) values were determined using the relation

$$V_{DC} = I_{DC} \times R_e$$

DC polarization measurements were performed on two samples, Li_6PS_5Br and $Li_{5.4}PS_{4.4}BrCl_{0.6}$ (Fig. 5d and e). Small voltages of 10, 20, 30, 40 and 50 mV were applied for 2 h each and the current values were recorded as a function of time. From the I-V curves shown in Fig. 5f and g, a clear linear relationship was observed between the applied voltage (V_{DC}) and the measured current (I_{DC}). The calculated resistance values from the slopes of these curves indicate an electronic resistance of 5.1 MΩ for Li_6PS_5Br, whereas $Li_{5.4}PS_{4.4}BrCl_{0.6}$ displays a lower resistance of 1.02 MΩ. The room temperature electronic conductivity was therefore determined as 3.3×10^{-8} S cm^{-1} for Li_6PS_5Br and 16.2×10^{-8} S cm^{-1} for $Li_{5.4}PS_{4.4}BrCl_{0.6}$. Although five times higher electronic conductivity is observed for $Li_{5.4}PS_{4.4}BrCl_{0.6}$, the value is still in a similar range as observed for other Li-argyrodites [12,60].

2.6. *Comparative electrochemical performances of $Li_{5.4}PS_{4.4}BrCl_{0.6}$ and Li_6PS_5Cl*

To evaluate the electrochemical performance of $Li_{5.4}PS_{4.4}BrCl_{0.6}$ (referred to as $\mathbf{Br_{10}Cl_6}$), all solid-state batteries were assembled using $LiNi_{0.6}Mn_{0.2}Co_{0.2}O_2$ (NMC-622) as the cathode active material and $Li_{0.5}In$-Li_6PS_5Cl (60-40 wt%) as the anode composite.

We have chosen two samples: the highly-conducting $Li_{5.4}PS_{4.4}BrCl_{0.6}$ composition isolated in this study ($Br_{10}Cl_6$) and a commercial Li_6PS_5Cl, widely utilized worldwide in ASSB research activities [61–63]. SEM micrographs of Li_6PS_5Cl, $Br_{10}Cl_6$ and NMC622 are shown in Fig. S5. While assembling the ASSBs, the cathode composite was prepared in a standard weight ratio of 70:30 of cathode: solid electrolyte, as often used (Kitaura et al. [64]). An optimal ratio is crucial to achieve optimal percolation in the composite cathode, ensuring the conduction pathways for ions and electrons and the composite microstructure, influencing both ionic and electronic conductivities, must be optimized to mitigate high tortuosity [65]. Whenever a new material has to be investigated, finding the optimal ratios of cathode and solid electrolyte becomes essential for ideal transport characteristics, as partial resistances within

the composite don't scale linearly with volume fractions of constituents [66].

As a first step, to choose the optimal weight ratio of SE and cathode active material in the catholyte, ASSBs were assembled with catholyte containing different weight ratio of NMC-622 and Br10Cl6. Catholyte powder made by manually grinding four distinct weight ratios of NMC-622 and Br10Cl6 (60-40, 70-30, 80-20 and 88-12 wt%) in an agate mortar and pestle. In all the cells, 20 mg of catholyte (different wt%), Br10Cl6 as separator and $Li_{0.5}In$-Li_6PS_5Cl (60-40 wt%) was used as anode composite. The ASSB fabrication pressure was 325 MPa, and a constant stack pressure (applied by torque wrench) of approximately 100 MPa was applied during electrochemical analyses.

The first charge-discharge cycles shown in Fig. 6a were conducted at a rate of C/30 and the upper cut-off voltage was set at 3.6 V vs. Li/LiIn. The initial specific charge capacities for all weight ratios of the catholyte are in the range of 179–185 mAh.g^{-1}, with an increasing trend observed as the ratio of NMC-622 increases, as shown in the inset of Fig. 6a. A columbic efficiency of 87 % is achieved for the ASSB with 60-40 wt% catholyte, while the batteries built with 70-30, 80-20, and 88-12 wt% of catholyte exhibit columbic efficiencies higher than 90 %. Notably, the columbic efficiencies are higher than those reported by Tarascon et al. [67] for NMC-622 and Li_6PS_5Cl, which were approximately 81 %. Although no significant difference is observed during the initial cycle at C/30, a notable difference becomes apparent when the cells are subjected to charge/discharge at different C rates (Fig. 6b). The ASSB with 88-12 wt% catholyte exhibits faster capacity fade, especially at higher C rates, while the ASSB with 70-30 wt% catholyte shows higher specific capacity over other cells at all C rates. Based on these observations, a catholyte with a 70-30 wt ratio of NMC-622 to solid electrolyte was selected as the optimal weight ratio to achieve the best electrochemical performance for later studies.

2.6.1. *Towards higher cathode active material loadings*

To achieve a practical ASSB with higher gravimetric energy density involves a ubiquitous strategy of increasing the cathode active material content of the positive electrode. Achieving better performance at higher loading of the cathode active material depends on several factors such as particle size distribution of cathode/solid electrolyte, tortuosity, etc; the ionic conductivity of the solid electrolyte also plays a crucial role [68]. To assess electrochemical performance at higher cathode loadings, ASSBs were assembled with a catholyte composition of 88-12 wt% of NMC-622 and Br10Cl6/Li_6PS_5Cl, allowing for a comparison. It is to be noted that specific capacities are calculated based on the mass of the cathode composite (around 20 mg).

The first charge-discharge cycle at C/30 of ASSB with catholyte containing different weight ratio of NMC-622 and Br10Cl6 are shown in Fig. 6c. This is basically the same data as in Fig. 6a, but represented in terms of total mass of the cathode composite. When the total mass of the cathode composite is considered, the initial charge capacities of 107.2 mAh.g^{-1}_{comp} is obtained for 60-40 wt% catholyte, whereas 88-12 wt % catholyte exhibits 166.2 mAh.g^{-1}_{comp} with a coulombic efficiency of 90 %. Under similar conditions, the ASSB with Li_6PS_5Cl delivers only 142 mAh.g^{-1}_{comp} with higher polarization and lower coulombic efficiency of 83.6 % (Fig. 6d). Although at higher C rates the capacity fade is faster in Br10Cl6, it can still deliver around 43 mAh.g^{-1}_{comp} at C/2, while Li_6PS_5Cl delivers only 11 mAh.g^{-1}_{comp}. To assess the long-term stability, both cells were subjected to charge/discharge at C/5 for 65 cycles. For the battery containing $Br_{10}Cl_6$ as the solid electrolyte, the specific discharge capacity decreased from 60.5 to 50.9 mAh.g^{-1}_{comp} (84.1 % retention) over 65 cycles, whereas in the case of Li_6PS_5Cl, the capacity decreases from 25.4 to 21.1 mAh.g^{-1}_{comp} (83 % retention) (Fig. 6d). Although both cells undergo significant capacity fade, $Br_{10}Cl_6$ exhibits much higher capacity compared to Li_6PS_5Cl even at cathode loading of 88 wt%. The overall improvement is ascribed to the higher ionic conductivity of $Br_{10}Cl_6$ which offers both higher ionic conductivity in cathode composite and facilitates faster ion transport in separator.

To deconvolute the effect of higher ionic conductivity in cathode composite and separator and to understand which factor affects most for the rate capability, four ASSBs were assembled in four different configurations (Fig. 7b).

(a) $Li_{0.5}In$-Li_6PS_5Cl | Br10Cl6 | Br10Cl6/NMC-622 (70-30 wt%)

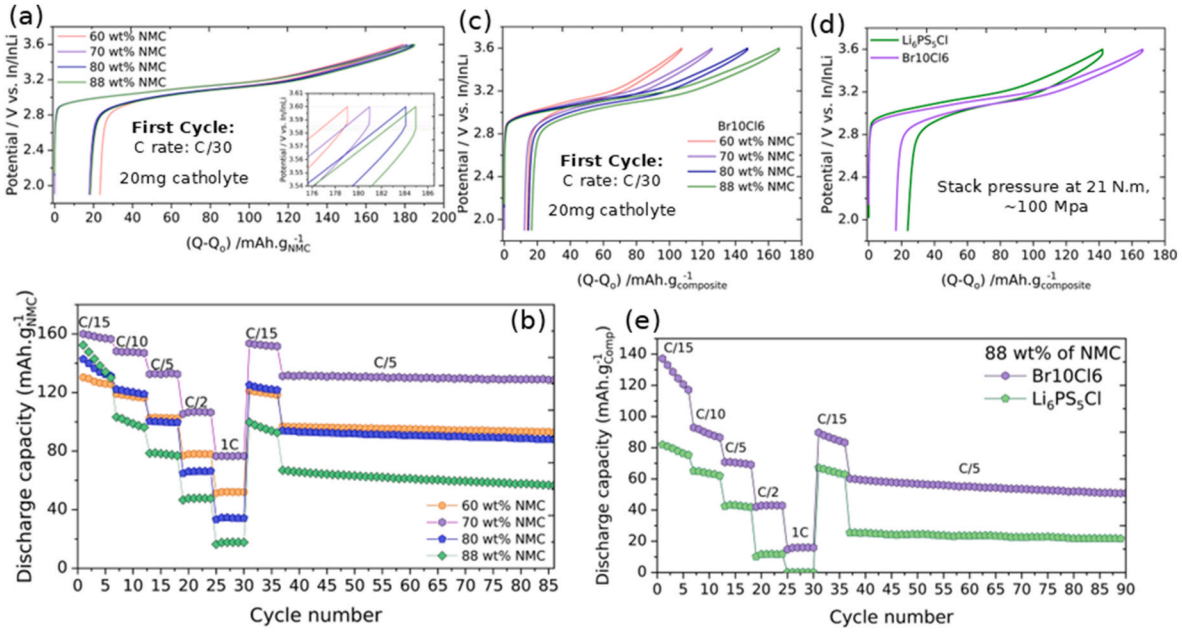

Fig. 6. Electrochemical performance of ASSBs assembled with catholyte of different wt % of NMC-622 and $Li_{5.4}PS_{4.4}BrCl_{0.6}$. (a) First charge/discharge cycle at C/30 (b) Discharge capacity at different C rates and long-term charge/discharge at C/5. (c) First charge discharge cycle at C/30 of ASSB with different weight ratio of NMC-622 and Br10Cl6 with capacity represented in terms of mass of cathode composite. ASSB cycling results for cathode composite in the weight ratio of 88-12 wt% of NMC-622 and $Li_{5.4}PS_{4.4}BrCl_{0.6}$/$Li_6PS_5Cl$ (d) Comparative first charge discharge cycles at C/30 of $Li_{5.4}PS_{4.4}BrCl_{0.6}$ and Li_6PS_5Cl then compared at different cycling rates in (e).

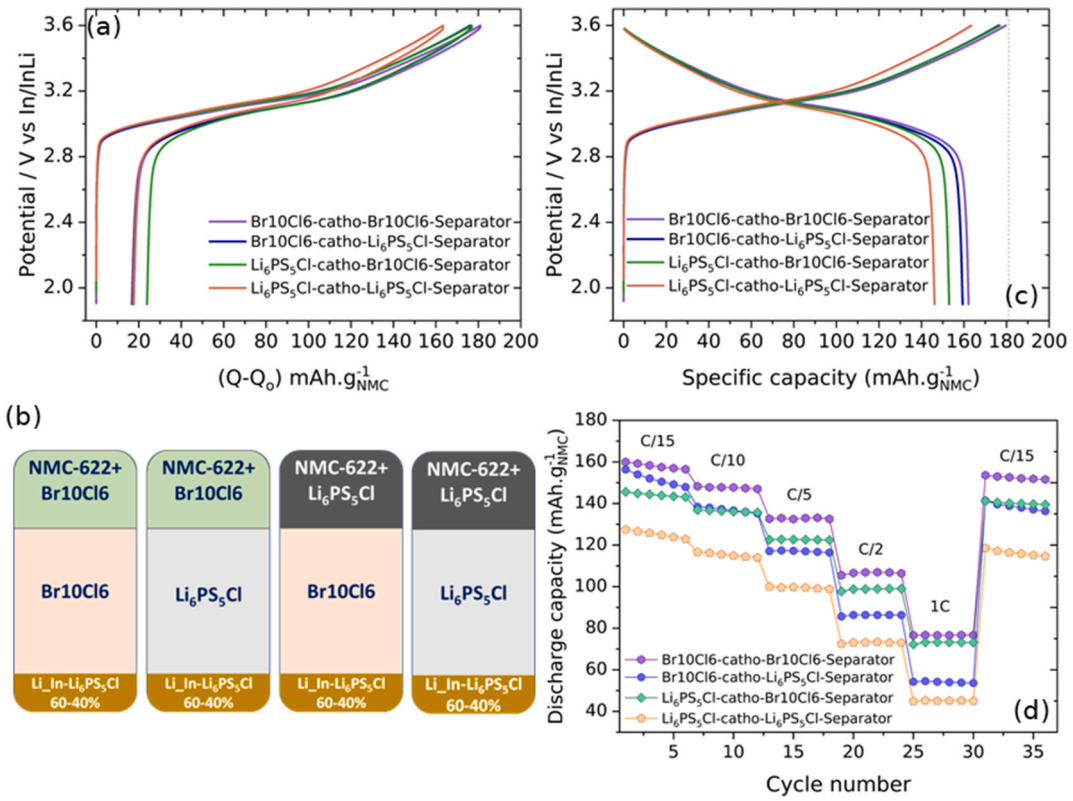

Fig. 7. (a) and (c) Galvanostatic charge/discharge curves at C/30 for the four ASSBs configurations depicted in (b). Br10Cl6 refers to $Li_{5.4}PS_{4.4}BrCl_{0.6}$. (d) Comparison of the rate capability of the four configurations.

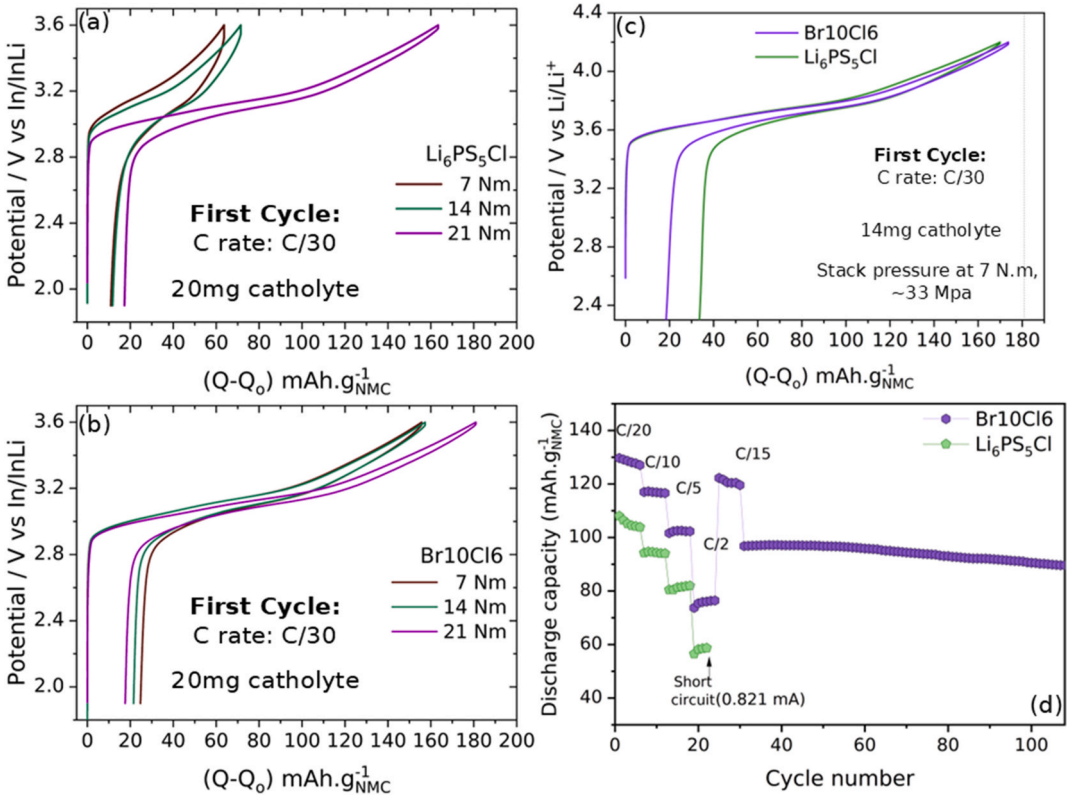

Fig. 8. Galvanostatic charge/discharge curves at C/30 for Li_6PS_5Cl at 3 different stack pressures for (a) Li_6PS_5Cl (b) $Li_{5.4}PS_{4.4}BrCl_{0.6}$ ASSB vs Li metal anode: Cycling results of $Li_{5.4}PS_{4.4}BrCl_{0.6}$ and Li_6PS_5Cl (c) First charge/discharge cycle at C/30 vs. Li metal and corresponding discharge capacity at different C rates and long-term charge/discharge at C/5 in (d).

(b) $Li_{0.5}In$-Li_6PS_5Cl | Li_6PS_5Cl | Br10Cl6/NMC-622 (70-30 wt%)
(c) $Li_{0.5}In$-Li_6PS_5Cl | Br10Cl6| Li_6PS_5Cl/NMC-622 (70-30 wt%)
(d) $Li_{0.5}In$-Li_6PS_5Cl | Li_6PS_5Cl | Li_6PS_5Cl/NMC-622 (70-30 wt%)

Galvanostatic charge/discharge curves at C/30 for 4 configurations are shown in Fig. 7a and c.

The 2 cells with $Br_{10}Cl_6$ in cathode composite deliver specific discharge capacity of 163.5 and 159.4 mAh.g^{-1} with coulombic efficiencies of ~90 %. While the 2 cells with Li_6PS_5Cl in cathode composite deliver specific discharge capacity of 152.4 and 145.1 mAh.g^{-1} with coulombic efficiency of 86.5 and 88.9 % respectively. Notably, the 2 cells with Br10Cl6 in the separator show higher specific capacity at higher C-rates. At 1C the 2 cells ((a) and (c)) with Br10Cl6 in the separator delivers the specific discharge capacity of 76.6 and 73.24 mAh.g^{-1}. These results suggest that at low C rates the limiting step is associated with the ionic conductivity of the cathode composite, while the ionic conductivity of the separator dominates the rate capability at higher C rates. Overall, the higher ionic conductivity of Br10Cl6 is favourable in the ASSBs compared to Li_6PS_5Cl.

2.7. Effect of stack pressure

So far, all the ASSBs we reported have been tested at a constant stack pressure of approximately 100 MPa, which corresponds to a torque of 21 Nm applied with a torque wrench. To evaluate the electrochemical performance of $Br_{10}Cl_6$ at lower stack pressures, three different ASSBs were assembled and the stack pressure of 100, 66 and 33 MPa were applied that corresponds to 21, 14 and 7 Nm torque (Fig. 8b). Similarly, ASSBs with Li_6PS_5Cl were also assembled for comparison and the galvanostatic charge/discharge curves at C/30 (Fig. 8a). At 33 MPa stack pressure, Li_6PS_5Cl shows low specific charge and discharge capacities of 63 and 51.9 mAh.g^{-1} and high polarization. Whereas under same conditions, $Br_{10}Cl_6$ delivers a specific charge and discharge capacities of 155 and 130.3 mAh.g^{-1} respectively. Even at 66 MPa the electrochemical performance of Li_6PS_5Cl is very low compared to $Br_{10}Cl_6$. Although at this point, we do not know the exact reason for this improvement, we suspect that there might be changes in the mechanical properties and the high ionic conductivity and moderate elastic modulus of $Br_{10}Cl_6$ that facilitates overall enhancement in the performance [69].

2.7.1. Performance of argyrodite electrolytes against lithium metal anode

ASSBs were assembled with lithium metal as the anode, considered to be the "Holy Grail" anode for use in ASSBs despite being extremely challenging due to issues related to the formation of Li dendrites, leading to internal short circuits. This issue stems from the inherent morphological instability during the plating and stripping of lithium metal at the SE separator interface [70]. Meng et al. [71] have demonstrated that controlling both fabrication and/or stack pressure play a crucial role during battery operation. However, controlling all the parameters was beyond the scope of this study, as our focus was solely on the comparative study of $Br_{10}Cl_6$ and Li_6PS_5Cl used under similar conditions.

ASSBs with Li metal were assembled using 14 mg of cathode composite (70-30 wt%) and 80 mg of solid electrolyte in the separator. These two layers were stacked, and a fabrication pressure of 375 MPa was applied for 3 min. Finally, a thin Li metal foil was attached to the other side, and a stack pressure of ~25 MPa was applied during electrochemical analyses. This specific stack pressure was determined after multiple trials within the range of 15–40 MPa. The initial charge-discharge cycles for $Br_{10}Cl_6$ and Li_6PS_5Cl, performed at a rate of at C/30 (54.7 μA g^{-1}) and with an upper cut-off voltage at 4.2 V vs. Li/Li$^+$ are shown in Fig. 8c and d. In the initial cycle, specific charge and discharge capacities of 173 and 153.1 mAh.g^{-1}, respectively, were attained for $Br_{10}Cl_6$, corresponding to a coulombic efficiency of 89.3 %. The ASSB incorporating Li_6PS_5Cl demonstrated comparable specific charge capacities of 170.3 mAh.g^{-1}. However, it exhibited a higher overpotential and a reduced specific discharge capacity of 136.6 mAh.g^{-1}, resulting in a coulombic efficiency of only 80 %. Even at different C rates, Br10Cl6 consistently delivers a higher capacity than Li_6PS_5Cl. At C/2 (0.821 mA g^{-1}), $Br_{10}Cl_6$ delivers 75.9 mAh.g-1, while Li_6PS_5Cl undergoes a short circuit after four cycles at C/2. This observation may be attributed to the higher critical current density of $Br_{10}Cl_6$, which impedes the formation of dendrites. To assess the long-term stability of the $Br_{10}Cl_6$ cell, it was subjected to charge/discharge at C/5 for 85 cycles. The specific discharge capacity at C/5 decreases from 96.7 to 89.6 mAh.g^{-1} with a capacity retention of 92.6 % retention over 85 cycles. The enhanced electrochemical performance can be attributed to the higher ionic conductivity and excellent stability of the Li/$Br_{10}Cl_6$ interface, as indicated by critical current density measurements.

To summarise the ASSB measurements, our comprehensive analysis conducted under various conditions consistently demonstrates that Br10Cl6 exhibits enhanced electrochemical performance when compared to commercial Li_6PS_5Cl.

3. Conclusions

This study investigates the structural and ionic transport properties of the $Li_{6-x}PS_{5-x}BrCl_x$ and $Li_{5.5}PS_{4.5}Br_{1.5-x}Cl_x$ argyrodite series using XRD, neutron diffraction, Raman spectroscopy, ^{31}P MAS NMR, impedance spectroscopy, and machine learning based MD simulations. The ionic conductivity of $Li_{5.4}PS_{4.4}BrCl_{0.6}$ reaches 9.8 mS cm^{-1} at 25 °C and remains notable at 1 mS cm^{-1} at −20 °C. The study identifies that the enhanced ionic conductivity arises from increased site disorder at the 4*d* and 4*a* sites and increased similarity between local lithium environments around the *4a* and *4d* sites contributing to a more uniform Li-ion hopping landscape; this is consistent with the experimental identification of T4 *16e* sites. Notably, solid-state batteries constructed with NMC-622 cathodes, $Li_{0.5}In$ anodes, and $Li_{5.4}PS_{4.4}BrCl_{0.6}$ electrolyte exhibit superior performance, including higher specific capacities, improved coulombic efficiencies, and better rate capabilities compared to the conventional electrolyte Li_6PS_5Cl. In addition, under various applied pressures and with lithium metal anodes, $Li_{5.4}PS_{4.4}BrCl_{0.6}$ demonstrates consistent electrochemical stability and exceptional cycling performance. These findings provide key insights into the role of halide substitution in improving ionic conductivity within the argyrodite structure. Further research into halogen-rich compositions could further enhance ionic conductivity and electrolyte stability, thereby accelerating the development and practical implementation of all-solid-state batteries.

4. Experimental and computational methods

Synthesis method: All the synthesis work and sample treatments were conducted in an argon-filled glovebox with O_2 and H_2O levels below 0.1 ppm. To synthesise both $Li_{6-x}PS_{5-x}BrCl_x$ ($0 \leq x \leq 0.8$) and $Li_{5.5}PS_{4.5}Br_{1.5-y}Cl_y$ ($0.0 \leq y \leq 1.5$) compositions, stoichiometric ratios of reagents, Li_2S (Sigma Aldrich, 99.98 %), P_2S_5 (Sigma Aldrich, 99 %) (3 wt% excess added), LiCl (Alfa Aesar, 99 %) and LiBr (Alfa Aesar, 99 %), were mixed to obtain 2g batches of precursors. The precursors were transferred into a Fritsch Pulverisette 7 premium line 80 mL zirconia ball-milling jar, along with 20 zirconia balls of 10 mm diameter (the ball-to-powder ratio was 30:1). Initially, the precursors were milled at 150 rpm for 30 min to homogenize the mixture. Ball milling was carried out at 600 rpm for 20 h in total. Each milling cycle consisted of 15 min of milling and 10 min of rest to dissipate the excess of heat. Throughout the milling process, the milling jars were periodically opened inside the glovebox, and any sample adhering to the walls and the cap was dislodged. After 20 h of ball milling, the obtained powder was pelletized into 10 mm pellets and sealed in quartz ampoules under vacuum of 10^{-2} mbar. Annealing was carried out at 450°C for 5 h, followed by normal cooling (2–3 °C/min). Finally, the annealed pellets were pulverized by grinding in a mortar and pestle and used for further characterization.

X-Ray Diffraction: XRD measurements of annealed powders were measured using a Bruker D8 Discover diffractometer equipped with CuKα radiation in reflection geometry for a 2θ range of 10°–50°, a step size of 0.02°, and a scan rate of 0.9 s/step. To mitigate sample sensitivity to moisture and air, PXRD data were collected using a custom airtight sample holder equipped with a Be window. Unit cell parameters were refined using the Le Bail fit method implemented in the FullProf software.

Neutron diffraction: Neutron powder diffraction experiments were conducted at the high-resolution powder diffractometer D2B beamline of the Institut Laue-Langevin (ILL), Grenoble, France. Approximately 2 g of sample was hermetically sealed in cylindrical vanadium containers. Diffraction data were collected at room temperature in transmission geometry and high intensity configuration without any collimation. A neutron wavelength of 1.594 Å was selected using the Ge(335) reflection from a germanium monochromator.

Solid-State NMR: NMR spectra were recorded on a Bruker Avance III HD spectrometer and a 17.6 T magnet operating at 303.6 MHz for ^{31}P, with a Bruker 4 mm triple resonance wide bore probe (used in double mode). The samples were packed into 4 mm zirconia rotors in an Ar-filled glovebox, sealed with a Kel- F cap and spun at the magic angle under dry nitrogen gas at a spinning rate of 10 kHz. One-pulse spectra were collected using a direct RF pulse of 4.75 us (52.6 kHz), setting the spectral width to 100 kHz and co-adding 64 transients. The recycling delays (d1) were set to 35–70s, chosen to be more than five times the longest measured longitudinal relaxation time for the PS_4^{3-} zone to ensure quantitative measurements. The FID were Fourier-transformed without apodization and all the spectra were referenced to 85 % H_3PO_4 at 0 ppm. The fits of the NMR spectra were performed with the dmfit software [72] after a baseline correction (spline on spectrum), using 10 Gaussian-shaped functions optimized on $Li_{5.7}PS_{4.7}BrCl_{0.3}$ and kept the same for the other samples except for the area. An additional broad Gaussian shaped function was necessary to obtain good fits, and its position, width and area were optimized individually for each sample. The contributions of the spinning sidebands were ignored as they did not modify the relative quantities of each peak significantly (similar anisotropies).

RAMAN Spectroscopy: Spectra were collected using a Raman DXR Microscope (Thermo Fischer Scientific) equipped with a green laser of excitation wavelength of 532 nm. A laser power of 0.1 mW was used to avoid sample damage due to excessive local heating. Spectra were collected by 1 s exposure time and 180 exposures.

Electrochemical Impedance Spectroscopy: Total conductivity was measured using AC impedance spectroscopy. About 200 mg of sample were uniaxially cold-pressed in a 10 mm die at 625 MPa. The relative density of the pellet was 85–87 % and the thickness was 1.4 mm approximately. Indium foils were pressed on the surface of pellets as ion-blocking electrodes. AC impedance spectroscopy was performed on these pellets by mounting them in BioLogic CESH cell and spectra were recorded using MTZ 35 frequency response analyzer by applying 50 mV AC perturbation in the frequency range from 30 MHz to 1 Hz. Spectra were collected between the temperature of range of −20 to 50 °C with 10 °C intervals in the ITS temperature controller. The AC impedance data were analyzed using Zview (Scribner)or RelaxIS software (rhd instruments, Darmstadt, Germany).

Critical current density measurement: Li | SE | Li symmetric cells were fabricated by densifying 150 mg of solid electrolyte powder at 375 MPa between two stainless steel pistons (10 mm diameter). Subsequently, Li metal foils (10 mm diameter) were pressed onto both sides of the solid electrolyte layer under a maintained uniaxial stack pressure of 25 MPa throughout operation. Electrochemical testing utilized a time-controlled measurement method, where a constant current was applied for 1 h during each charge and discharge cycle. The current density was initially set at 0.05 mA/cm^2 and incrementally increased until short-circuit failure was observed.

Cell fabrication: The cathode composite was prepared by grinding 70 wt% of $LiNi_{0.6}Mn_{0.2}Co_{0.2}O_2$ (NMC-622) and 30 wt% of solid electrolyte for 20 min. In specific cases, the cathode composition was adjusted as indicated in the respective sections. The anode composite was obtained by grinding a 60:40 wt% ratio of $Li_{0.5}In$ alloy and Li_6PS_5Cl for 1 h to form a dark grey powder. To assemble the battery, approximately 49 mg of solid electrolyte (SE) powder was introduced into a 10 mm polymer mold and densified by cold pressing under 125 MPa for 1 min. Subsequently, 20–22 mg of the cathode composite (containing 14–15 mg NMC-622) was uniformly layered on one side of the solid electrolyte, while 85 mg of the anode composite was applied to the opposite side. The stack was pressed at 375 MPa for 5 min, assembled into a stainless-steel frame, and subjected to a uniaxial stack pressure of 100 MPa using a torque wrench.

First-principles calculations: Density-functional theory (DFT) calculations were used to train a machine-learning interatomic potential (MLIP) for argyrodites spanning the composition space from Li_7PS_6 to $Li_5PS_4Cl_2$ and $Li_5PS_4Br_2$. Training structures were sampled from ab initio molecular dynamics and single-point calculations using VASP [73] and the projector-augmented wave method [74,75]. The strongly constrained and appropriately normed (SCAN) functional with the revised Vydrov-van Voorhees dispersion correction [76] (rVV10) were used, with a plane-wave cutoff of 600 eV and k-point spacing 0.25 Å^{-1}. The convergence cutoff for energy was 10^{-6} eV with an "accurate" precision setting. Ab initio molecular dynamics (AIMD) were carried out at temperatures between 300 K and 1200 K in isobaric and isovolumetric ensembles at compositions spanning the above chemical space. Enhanced sampling was used to improve sampling of lithium hopping and stresses. The same settings were used for single-point calculations during active learning loops.

MLIP settings and training: the equivariant graph neural network architecture *allegro* [77] was used to train the MLIP (nequip 0.6.1) [78,79]. For all models, the key network parameters were 5 Å radial cutoff and tensorial feature maximum dimension $l_{max} = 1$ with initial embedding multiplicity 32 and final edge layer 128. The dimensions of the two-body perceptron layers were 64, 128, 256, and 256, and those of the latent perceptron layers 256, 256, and 256. The training with starting learning rate 0.005 was conducted on one NVIDIA A100 GPU per model for up to 1 day. Uncertainty was estimated in active learning cycles as the standard deviation of predicted force components a committee of models. The model was evaluated on a fully out-of-distribution test set of stoichiometries (Br/Cl) not seen during training and whose configurations were sampled from AIMD at 600k, the *allegro* model reproduces SCAN-DFT reference data (retroactively) with an energy RMSE of 0.0021 eV atom^{-1} (MAE 0.0020 eV atom^{-1}, R = 0.9952) and a force RMSE of 0.0714 eV Å^{-1} atom^{-1} (MAE 0.0527 eV Å^{-1} atom^{-1}, R = 0.9942), while element-resolved force RMSEs remain low—0.0499 eV Å^{-1} atom^{-1} for Li, 0.1346 eV Å^{-1} atom^{-1} for P, 0.0785 eV Å^{-1} atom^{-1} for S, 0.0516 eV Å^{-1} atom^{-1} for Br, and 0.0537 eV Å^{-1} atom^{-1} for Cl.

Molecular dynamics (MD) simulations: The *allegro* model was used in LAMMPS [80] for MD simulations of $Li_{6-x}PS_{5-x}BrCl_x$ for x = 0,0.3, 0.6 at 323 K. The simulations used a 3 × 3 × 3 supercell of the conventional unit cell. The occupancies of the Wyckoff 4a and 4d sites were the same as in Fig. 2(cd). No other ordering or correlations were assumed: the cage-center sites were populated randomly in accordance with the experimentally determined occupancies. Constant-pressure simulations were carried out with a timestep of 5 fs for 45–90 ns (which is much longer than typical AIMD simulations of 100ps). To calculate the vibrational density of states as a fast proxy for spectroscopic observables, velocity autocorrelation functions were computed up to 50 ps in time lag. The lithium ionic conductivity was calculated by window-averaging the center-of-mass mean-square displacement for log-spaced time lags up to 10 ns, equivalent to 100 MHz. Since the conductivities at 1–10 ns (1 GHz–100 MHz) were independent of frequency, they were averaged to represent the d.c. conductivity.

Simulation of ^{31}P NMR spectra: NMR shifts were computed from structures sampling all 15 arrangements of S, Br, and Cl on 4d sites

adjacent to a PS_4 polyhedron. For each set of 4d neighbours of a PS_4 tetrahedron, every possible configuration of 4a neighbours was also considered. Structures used for NMR calculations were of size 1 conventional unit cell. Lithium positions were randomized via isobaric molecular dynamics and sample structures were relaxed. The NMR magnetic shielding tensors were calculated with the CASTEP 23.11 plane-wave pseudopotential code using the GIPAW approach [81]. All calculations used ultrasoft pseudopotentials with a cutoff energy 900 eV and k-point spacing 0.05 $Å^{-1}$ for sampling the Brillouin zone. For these values the ^{31}P isotropic shifts for individual atoms were converged to within 1 ppm. All calculations used the PBE functional, which has been shown to generally give good agreement with experiment [82]. Arbitrary reference shieldings, σ_{ref}, are required to convert NMR shieldings, σ, to chemical shifts, δ, viz. $\delta = \sigma_{ref} - \sigma$. The reference shieldings were determined by taking the intercept of a linear fit of a set of experimental δ_{iso} and calculated σ_{iso} values for a diverse set of reference compounds.

CRediT authorship contribution statement

Dhanush Shanbhag: Writing – review & editing, Writing – original draft, Investigation, Formal analysis, Data curation, Conceptualization. **Ajay Gautam:** Formal analysis. **Elodie Salager:** Writing – review & editing, Investigation, Formal analysis, Data curation. **Laura Albero-Blanquer:** Writing – review & editing, Supervision, Investigation, Funding acquisition. **Florencia Marchini:** Writing – review & editing, Validation, Supervision, Investigation, Funding acquisition, Conceptualization. **Jean-Noël Chotard:** Writing – review & editing, Investigation, Formal analysis, Data curation. **François Fauth:** Writing – review & editing, Formal analysis, Data curation. **Emmanuelle Suard:** Writing – review & editing, Investigation, Formal analysis, Data curation. **François Rabuel:** Writing – review & editing, Investigation, Data curation, Conceptualization. **Houssny Bouyanfif:** Writing – review & editing, Investigation, Formal analysis, Data curation. **Andrey D. Poletayev:** Writing – review & editing, Methodology, Investigation, Formal analysis, Conceptualization. **Christopher Davies:** Writing – review & editing, Methodology, Investigation, Formal analysis, Data curation. **Benjamin Zelin:** Writing – review & editing, Methodology, Investigation, Formal analysis, Conceptualization. **M. Saiful Islam:** Writing – review & editing, Methodology, Investigation, Funding acquisition, Formal analysis, Conceptualization. **Virginie Viallet:** Writing – review & editing, Supervision, Project administration, Methodology, Investigation, Funding acquisition, Conceptualization. **Christian Masquelier:** Writing – review & editing, Supervision, Project administration, Investigation, Funding acquisition, Conceptualization.

Declaration of competing interest

The authors declare the following financial interests/personal relationships which may be considered as potential competing interests: Dhanush Shanbhag reports financial support was provided by UMICORE Group Research and Development. If there are other authors, they declare that they have no known competing financial interests or personal relationships that could have appeared to influence the work reported in this paper.

Acknowledgement

D.S. and C.M. gratefully acknowledges UMICORE for financial support provided through a joint Ph.D. project between with LRCS. The authors thank the Institut Laue-Langevin (ILL) for beam time allocation on the D2B diffractometer for powder diffraction measurements, the ALBA synchrotron for beam time on the MSPD diffractometer, and CEMHTI (Orléans) for access to solid-state NMR facilities. Computational work was carried out using the UK Materials and Molecular Modelling Hub, which is partially funded by EPSRC (EP/T022213/1, EP/W032260/1 and EP/P020194/1) and the ARCHER2 high-performance computing facility through the HEC Materials Chemistry Consortium (EP/R029431). A.D.P. and S.I. gratefully acknowledgce the Faraday Institution (EP/S003053/1, FIRG016).

Appendix A. Supplementary data

Supplementary data to this article can be found online at https://doi.org/10.1016/j.jpowsour.2025.238175.

Data availability

Data will be made available on request.

References

[1] Y. Chen, et al., A review of lithium-ion battery safety concerns: the issues, strategies, and testing standards, J. Energy Chem. 59 (2021) 83–99.
[2] J.B. Goodenough, Y. Kim, Challenges for rechargeable li batteries, Chem. Mater. 22 (2010) 587–603.
[3] J.-M. Tarascon, M. Armand, Issues and challenges facing rechargeable lithium batteries, Nature 414 (2001) 359–367.
[4] J. Janek, W.G. Zeier, A solid future for battery development, Nat. Energy 1 (2016) 1–4.
[5] J. Janek, W.G. Zeier, Challenges in speeding up solid state battery development, Nat. Energy 8 (2023) 230–240.
[6] J.C. Bachman, et al., Inorganic solid-state electrolytes for lithium batteries: mechanisms and properties governing ion conduction, Chem. Rev. 116 (2016) 140–162.
[7] T. Famprikis, P. Canepa, J.A. Dawson, M.S. Islam, C. Masquelier, Fundamentals of inorganic solid-state electrolytes for batteries, Nat. Mater. 18 (2019) 1278–1291.
[8] X. Li, et al., Air-stable Li3InCl6 electrolyte with high voltage compatibility for all-solid-state batteries, Energy Environ. Sci. 12 (2019) 2665–2671.
[9] Y. Tanaka, et al., New oxyhalide solid electrolytes with high lithium ionic conductivity >10 mS cm−1 for all-solid-state batteries, Angew. Chemie Int. Ed. 62 (2023) e202217581.
[10] J. Park, et al., NaAlCl4: new halide solid electrolyte for 3 V stable cost-effective all-solid-state Na-Ion batteries, ACS Energy Lett. 7 (2022) 3293–3301.
[11] L. Zhou, N. Minafra, W.G. Zeier, L.F. Nazar, Innovative approaches to Li-Argyrodite solid electrolytes for all-solid-state lithium batteries, Acc. Chem. Res. 54 (2021) 2717–2728.
[12] H.J. Deiseroth, et al., Li 7PS 6 and li 6PS 5X (X: cl, Br, I): possible three-dimensional diffusion pathways for lithium ions and temperature dependence of the ionic conductivity by impedance measurements, Zeitschrift fur Anorg. und Allg. Chemie 637 (2011) 1287–1294.
[13] S. Boulineau, M. Courty, J.M. Tarascon, V. Viallet, Mechanochemical synthesis of Li-argyrodite li 6PS 5X (X = Cl, Br, I) as sulfur-based solid electrolytes for all solid state batteries application, Solid State Ionics 221 (2012) 1–5.
[14] M.A. Kraft, et al., Influence of lattice polarizability on the ionic conductivity in the lithium superionic argyrodites Li6PS5X (X = Cl, Br, I), J. Am. Chem. Soc. 139 (2017) 10909–10918.
[15] H. Al-Kutubi, et al., Decoding structural disorder, synthesis methods, and Short- and long-range lithium-ion transport in lithium argyrodites (Li6–xPS5–xBr1+x), Chem. Mater. 37 (2025) 869–883.
[16] J. Hartel, et al., Investigating the influence of transition metal substitution in lithium argyrodites on structure, transport, and solid-state battery performance, Chem. Mater. 36 (2024) 10731–10745.
[17] M.J. Fallon, et al., Exploring the anion site disorder kinetics in lithium argyrodites, J. Am. Chem. Soc. 147 (2025) 10151–10159.
[18] A. Gautam, M. Ghidiu, E. Suard, M.A. Kraft, W.G. Zeier, On the lithium distribution in halide superionic argyrodites by halide incorporation in Li7-xPS6-xClx, ACS Appl. Energy Mater. 4 (2021) 7309–7315.
[19] N. Minafra, et al., Local charge inhomogeneity and lithium distribution in the superionic argyrodites Li6PS5X (X = Cl, Br, I), Inorg. Chem. 59 (2020) 11009–11019.
[20] A. Gautam, et al., Engineering the site-disorder and lithium distribution in the lithium superionic argyrodite Li6PS5Br, Adv. Energy Mater. Ahead of Print (2020), https://doi.org/10.1002/aenm.202003369.
[21] N.J.J. De Klerk, I. Rosłoń, M. Wagemaker, Diffusion mechanism of li argyrodite solid electrolytes for Li-Ion batteries and prediction of optimized halogen doping: the effect of li vacancies, halogens, and halogen disorder, Chem. Mater. 28 (2016) 7955–7963.
[22] H.-J. Lee, et al., Lithium localization by anions in argyrodite solid electrolytes from Machine-Learning-based simulations, Adv. Energy Mater. 14 (2024) 2402396.
[23] S. Ohno, et al., Further evidence for energy landscape flattening in the superionic argyrodites Li6+ xP1- xMxS5I (M = Si, Ge, sn), Chem. Mater. 31 (2019) 4936–4944.
[24] M.A. Kraft, et al., Inducing high ionic conductivity in the lithium superionic argyrodites Li6+xP1-xGexS5I for all-solid-state batteries, J. Am. Chem. Soc. 140 (2018) 16330–16339.
[25] L. Zhou, A. Assoud, Q. Zhang, X. Wu, L.F. Nazar, New family of argyrodite thioantimonate lithium superionic conductors, J. Am. Chem. Soc. 141 (2019) 19002–19013.

[26] J. Du, et al., Electrochemical testing and benchmarking of compositionally complex lithium argyrodite electrolytes for all-solid-state battery application, Batter. Supercaps 7 (2024) e202400112.
[27] L. Peng, C. Yu, S. Cheng, J. Xie, Halogen-rich lithium argyrodite solid-state electrolytes: a review, Batter. Supercaps 6 (2023).
[28] S.V. Patel, et al., Tunable lithium-ion transport in mixed-halide argyrodites li 6– x PS 5– x ClBr x : an unusual compositional space, Chem. Mater. 33 (2021) 1435–1443.
[29] P. Adeli, et al., Boosting solid-state diffusivity and conductivity in lithium superionic argyrodites by halide substitution, Angew. Chem. Int. Ed. 58 (2019) 8681–8686.
[30] X. Feng, et al., Enhanced ion conduction by enforcing structural disorder in Li-deficient argyrodites Li6−xPS5−xCl1+x, Energy Storage Mater. 30 (2020) 67–73.
[31] T.T. Zuo, et al., Impact of the chlorination of lithium argyrodites on the electrolyte/cathode interface in solid-state batteries, Angew. Chem. Int. Ed. 202213228 (2022).
[32] P. Wang, et al., Fast ion conduction and its origin in Li6- xPS5- xBr1+ x, Chem. Mater. 32 (2020) 3833–3840.
[33] A. Gautam, H. Al-Kutubi, T. Famprikis, S. Ganapathy, M. Wagemaker, Exploring the relationship between halide substitution, structural disorder, and lithium distribution in lithium argyrodites (Li6-xPS5-xBr1+x), Chem. Mater. 35 (2023) 8081–8091.
[34] Z. Zhang, et al., Iodine-rich lithium argyrodite with enhanced ionic conductivity for solid-state batteries, Scr. Mater. 210 (2022) 114475.
[35] N. Masuda, K. Kobayashi, F. Utsuno, T. Uchikoshi, N. Kuwata, Effects of halogen and sulfur mixing on lithium-ion conductivity in Li7- x- y(PS4)(S2- x- yClxBry) argyrodite and the mechanism for enhanced lithium conduction, J. Phys. Chem. C (2022) 4–11, https://doi.org/10.1021/acs.jpcc.2c03780.
[36] S. Li, et al., High-entropy lithium argyrodite solid electrolytes enabling stable all-solid-state batteries, Angew. Chem. Int. Ed. (2023), https://doi.org/10.1002/anie.202314155.
[37] H. Yan, et al., Synergy of I-Cl co-occupation on halogen-rich argyrodites and resultant dual-layer interface for advanced all-solid-state li metal batteries, J. Energy Chem. 86 (2023) 499–509.
[38] Y. Subramanian, R. Rajagopal, K.S. Ryu, Synthesis, air stability and electrochemical investigation of lithium superionic bromine substituted argyrodite (Li6-xPS5-xCl1.0Brx) for all-solid-state lithium batteries, J. Power Sources 520 (2022) 230849.
[39] WO2020/033809 A1..
[40] A.K. Lavrinenko, et al., Optimizing ionic transport in argyrodites: a unified view on the role of sulfur/halide distribution and local environments, J. Mater. Chem. A 12 (2024) 26596–26611.
[41] A. Gautam, et al., Rapid crystallization and kinetic freezing of site-disorder in the lithium superionic argyrodite Li6PS5Br, Chem. Mater. 31 (2019) 10178–10185.
[42] Y. Zhou, et al., Observation of interfacial degradation of li 6 PS 5 Cl against lithium metal and LiCoO 2 via in situ electrochemical raman microscopy, Batter. Supercaps 3 (2020) 647–652.
[43] A. Müller, N. Mohan, P. Cristophliemk, I. Tossidis, M. Dräger, Investigation of the vibrational spectra of PS43−, CS32−, CS2Se2−, CSSe22−, CSe32−, BCl2Br and BClBr2, Spectrochim. Acta Part A Mol. Spectrosc. 29 (1973) 1345–1356.
[44] T. Famprikis, et al., Insights into the rich polymorphism of the na+ ion conductor Na3PS4 from the perspective of variable-temperature diffraction and spectroscopy, Chem. Mater. 33 (2021) 5652–5667.
[45] C. Dietrich, et al., Lithium ion conductivity in Li2S–P2S5 glasses – building units and local structure evolution during the crystallization of superionic conductors Li3PS4, Li7P3S11 and Li4P2S7, J. Mater. Chem. A 5 (2017) 18111–18119.
[46] H.J. Deiseroth, et al., Li6PS5X: a class of crystalline Li-rich solids with an unusually high li+ mobility, Angew. Chem. Int. Ed. 47 (2008) 755–758.
[47] R. Schlenker, et al., Structure and diffusion pathways in Li6PS5Cl argyrodite from neutron diffraction, pair-distribution function analysis, and NMR, Chem. Mater. 32 (2020) 8420–8430.
[48] P. Wang, et al., Configurational and dynamical heterogeneity in superionic Li5.3PS4.3Cl1.7−Br, Adv. Funct. Mater. 33 (2023) 2307954.
[49] Zelin Benjamin, A Computationally Efficient Study of the Effects of Dynamics on First Principles NMR Calculations in Solid Electrolytes, University of Oxford, 2024.
[50] A. Banerjee, et al., Na3SbS4: a solution processable sodium superionic conductor for all-solid-state sodium-ion batteries, Angew. Chemie Int. Ed. 55 (2016) 9634–9638.
[51] B.J. Morgan, Mechanistic origin of superionic lithium diffusion in anion-disordered Li6PS5X argyrodites, Chem. Mater. 33 (2021) 2004–2018.
[52] Z. Sun, et al., Insights on the properties of the O-Doped argyrodite sulfide solid electrolytes (Li6PS5- xClOx,x=0-1), ACS Appl. Mater. Interfaces 13 (2021) 54924–54935.
[53] B.W. Taklu, et al., Dual CuCl doped argyrodite superconductor to boost the interfacial compatibility and air stability for all solid-state lithium metal batteries, Nano Energy 90 (2021) 106542.
[54] W. Xiao, et al., Stable all-solid-state battery enabled with Li6.25PS5.25Cl0.75 as fast ion-conducting electrolyte, J. Energy Chem. 53 (2020) 147–154.
[55] Y. Lee, et al., Superionic Si-Substituted lithium argyrodite sulfide electrolyte Li6+ xSb1- xSi xS5I for all-solid-state batteries, ACS Sustain. Chem. Eng. 9 (2021) 120–128.
[56] D. Zeng, et al., Promoting favorable interfacial properties in lithium-based batteries using chlorine-rich sulfide inorganic solid-state electrolytes, Nat. Commun. 13 (2022) 1909.
[57] R. Song, et al., Metastable decomposition realizing dendrite-free solid-state li metal batteries, Adv. Energy Mater. 13 (2023) 2203631.
[58] He, B. et al. Halogen Chemistry of Solid Electrolytes in all-solid-state Batteries. doi: 10.1038/s41570-023-00541-7..
[59] H. Guo, et al., High-entropy sulfide argyrodite electrolytes for all-solid-state lithium-sulfur batteries, Cell Rep. Phys. Sci. 5 (2024).
[60] P. Gorai, T. Famprikis, B. Singh, V. Stevanović, P. Canepa, Devil is in the defects: electronic conductivity in solid electrolytes, Chem. Mater. 33 (2021) 7484–7498.
[61] F.J. Simon, M. Hanauer, A. Henss, F.H. Richter, J. Janek, Properties of the interphase formed between argyrodite-type Li6PS5Cl and polymer-based PEO10: LiTFSI, ACS Appl. Mater. Interfaces 11 (2019) 42186–42196.
[62] E. Quemin, et al., Decoupling parasitic reactions at the positive electrode interfaces in argyrodite-based systems, ACS Appl. Mater. Interfaces 14 (2022) 49284–49294.
[63] P. Minnmann, L. Quillman, S. Burkhardt, F.H. Richter, J. Janek, Editors' choice—quantifying the impact of charge transport bottlenecks in composite cathodes of all-solid-state batteries, J. Electrochem. Soc. 168 (2021) 040537.
[64] H. Kitaura, A. Hayashi, T. Ohtomo, S. Hama, M. Tatsumisago, Fabrication of electrode–electrolyte interfaces in all-solid-state rechargeable lithium batteries by using a supercooled liquid state of the glassy electrolytes, J. Mater. Chem. 21 (2011) 118–124.
[65] G.F. Dewald, S. Ohno, J.G.C. Hering, J. Janek, W.G. Zeier, Analysis of charge carrier transport toward optimized cathode composites for all-solid-state li−S batteries, Batter. Supercaps 4 (2021) 183–194.
[66] T. Hendriks, M. Lange, E. Kiens, C. Baeumer, W. Zeier, Balancing partial ionic and electronic transport for optimized cathode utilization of high-voltage LiMn2O4/Li3InCl6 solid-state batteries, Batter. Supercaps (2023), https://doi.org/10.1002/batt.202200544.
[67] T. Koç, F. Marchini, G. Rousse, R. Dugas, J.-M. Tarascon, In search of the best solid electrolyte-layered oxide pairing for assembling practical all-solid-state batteries, ACS Appl. Energy Mater. 4 (2021) 13575–13585.
[68] M. Cronau, M. Duchardt, M. Szabo, B. Roling, Ionic conductivity versus particle size of ball-milled sulfide-based solid electrolytes: strategy towards optimized composite cathode performance in all-solid-state batteries, Batter. Supercaps 202200041 (2022) 2–7.
[69] Y.J. Kim, S. Nahm, J.-H. Lee, H. Kim, Comprehensive analysis of halogen-rich argyrodite sulfides from a multi-level perspective: li-ion conduction and elastic modulus, ACS Mater. Lett. 7 (2025) 724–729.
[70] J. Janek, W.G. Zeier, Challenges in speeding up solid-state battery development, Nat. Energy 8 (2023) 230–240.
[71] J.M. Doux, et al., Pressure effects on sulfide electrolytes for all solid-state batteries, J. Mater. Chem. A 8 (2020) 5049–5055.
[72] D. Massiot, et al., Modelling one- and two-dimensional solid-state NMR spectra, Magn. Reson. Chem. 40 (2002) 70–76.
[73] G. Kresse, J. Hafner, Ab initio molecular dynamics for liquid metals, Phys. Rev. B 47 (1993) 558–561.
[74] P.E. Blöchl, Projector augmented-wave method, Phys. Rev. B 50 (1994) 17953–17979.
[75] J. Sun, A. Ruzsinszky, J.P. Perdew, Strongly constrained and appropriately normed semilocal density functional, Phys. Rev. Lett. 115 (2015) 36402.
[76] H. Peng, Z.-H. Yang, J.P. Perdew, J. Sun, Versatile van der Waals Density Functional Based on a Meta-Generalized Gradient Approximation, Phys. Rev. X 6 (2016) 41005.
[77] A. Musaelian, et al., Learning local equivariant representations for large-scale atomistic dynamics, Nat. Commun. 14 (2023) 579.
[78] M. Geiger, T. Smidt, e3nn: euclidean neural networks, arXiv2207.09453 (2022) 1–22.
[79] S. Batzner, et al., E(3)-equivariant graph neural networks for data-efficient and accurate interatomic potentials, Nat. Commun. 13 (2022) 2453.
[80] A.P. Thompson, et al., LAMMPS - a flexible simulation tool for particle-based materials modeling at the atomic, meso, and continuum scales, Comput. Phys. Commun. 271 (2022) 108171.
[81] J.R. Yates, C.J. Pickard, F. Mauri, Calculation of NMR chemical shifts for extended systems using ultrasoft pseudopotentials, Phys. Rev. B 76 (2007) 24401.
[82] C. Bonhomme, et al., First-principles calculation of NMR parameters using the gauge including projector augmented wave method: a chemist's point of view, Chem. Rev. 112 (2012) 5733–5779.